

## University of Tasmania Open Access Repository

### Cover sheet

**Title**

Petrogenetic variability along the North-South Propagating Spreading Center of the North Fiji Basin

**Author**

Fleutelot, C, Eissen, JP, Dosso, L, Juteau, T, Launeau, P, Bollinger, C, Cotten, J, Leonid Danyushevsky, Savoyant, L

**Bibliographic citation**

Fleutelot, C; Eissen, JP; Dosso, L; Juteau, T; Launeau, P; Bollinger, C; et al. (2005). Petrogenetic variability along the North-South Propagating Spreading Center of the North Fiji Basin. University Of Tasmania. Journal contribution.

[https://figshare.utas.edu.au/articles/journal\\_contribution/Petrogenetic\\_variability\\_along\\_the\\_North-South\\_Propagating\\_Spreading\\_Center\\_of\\_the\\_North\\_Fiji\\_Basin/22856270](https://figshare.utas.edu.au/articles/journal_contribution/Petrogenetic_variability_along_the_North-South_Propagating_Spreading_Center_of_the_North_Fiji_Basin/22856270)

Is published in: [10.1007/s00710-004-0061-5](https://doi.org/10.1007/s00710-004-0061-5)

**Copyright information**

This version of work is made accessible in the repository with the permission of the copyright holder/s under the following,

**Licence.**

If you believe that this work infringes copyright, please email details to: [oa.repository@utas.edu.au](mailto:oa.repository@utas.edu.au)

Downloaded from [University of Tasmania Open Access Repository](#)

Please do not remove this coversheet as it contains citation and copyright information.

University of Tasmania Open Access Repository

Library and Cultural Collections

University of Tasmania

Private Bag 3

Hobart, TAS 7005 Australia

E [oa.repository@utas.edu.au](mailto:oa.repository@utas.edu.au)

CRICOS Provider Code 00586B | ABN 30 764 374 782

[utas.edu.au](http://utas.edu.au)

## **Petrogenetic variability along the North–South Propagating Spreading Center of the North Fiji Basin**

**C. Fleutelot<sup>1</sup>, J.-P. Eissen<sup>2</sup>, L. Dosso<sup>3</sup>, T. Juteau<sup>1</sup>, P. Launeau<sup>4</sup>,  
C. Bollinger<sup>3</sup>, J. Cotten<sup>1</sup>, L. Danyushevsky<sup>5</sup>, and L. Savoyant<sup>6</sup>**

<sup>1</sup> UMR 6538 “Domaines Océaniques”, Université de Bretagne Occidentale,  
Brest, France

<sup>2</sup> IRD, UR 163 “Processus et Aléas Volcaniques”, Clermont-Ferrand, France

<sup>3</sup> UMR 6538 “Domaines Océaniques”, Ifremer, Plouzané, France

<sup>4</sup> UPRES-EA 2156, Laboratoire de Pétrologie Structurale, Université de Nantes,  
Nantes, France

<sup>5</sup> Department of Geology, University of Tasmania, Hobart, Australia

<sup>6</sup> UMR 5569 “Géofluides, Bassins, Eau”, Université de Montpellier II,  
Montpellier, France

Received February 20, 2003; revised version accepted August 25, 2004

Published online November 3, 2004; © Springer-Verlag 2004

Editorial handling: J. G. Raith

### **Summary**

Previous studies on propagating rifts suggested that segmentation of a spreading axis could represent the superficial mark of mantle behavior (*Sinton et al.*, 1983; *Nicolas*, 1989; *Gente et al.*, 1995). The study of North–South Propagating Spreading Center (NS-PSC) from the North Fiji Basin (NFB) brings new insights to this debate. Basalts from the central part of the propagator have more variable incompatible and isotopic ratios than those from its northern tip. A model of dynamic partial melting of a thermally and slightly geochemically and isotopically heterogeneous mantle is proposed. Beneath the central segment, the partial fusion starts deeper (ca. 30 km) and reaches a higher rate (ca. 22%). Further open system differentiation occurs within shallow permanent magma reservoirs along most of the central segment. Below the segment closest to the tip of the propagator the partial fusion starts shallower (ca. 25 km) and stays at a lower rate (ca. 16%). The maximum of differentiation occurs close to the propagator, in small, periodically disconnected, magma bodies resulting in the production of ferrobasalts close to the tip. In order to explain these variations, the presence of an asthenospheric diapir focused beneath the central part of the NS-PSC is proposed. The petrogenetic processes of propagating spreading centers of mature oceanic basins or back-arc basins are identical.

## Introduction

Propagating spreading centers (called PSC hereafter) were first described by Hey (1977). PSCs are limited by pseudofaults with a V-shaped pointing toward the sense of the migration of a spreading axis. The pseudofaults limit two different portions of oceanic crust: younger one generated at the axis of the propagating spreading center and older one into which the PSC migrates. The newly accreted portion of PSC crust can then be defined by the magnetic anomalies parallel to the axis (Hey and Sinton, 1979; Hey et al., 1980; Johnson et al., 1983; Phipps Morgan and Parmentier, 1985; Wilson and Hey, 1995). Following this definition, different types of PSCs have been described throughout the oceans: i) “Type 1” are up to 1000 km long, *e.g.* Galapagos spreading centers (Hey et al., 1986) and Reykjanes, Pacific-Antarctic, Australia-Antarctic (Gilg-Capar, 1994); ii) “Type 2” are 100–300 km long, *e.g.* Juan de Fuca ridge (Hey and Wilson, 1982), the North–South PSC from the North Fiji Basin (de Altermann et al., 1993; Ruellan et al., 1994), and the Lau Basin (Parson et al., 1990), and iii) “Type 3” are 50–80 km long, *e.g.* the rhomboedric structures from the Mid Atlantic Ridge (Lewis, 1979; Gente et al., 1995). PSCs exist in all oceanic basins, independent of spreading rate or geodynamic settings *e.g.* back-arc basins or mature oceanic basins.

Previous petrogenetical studies on propagating rifts (Christie and Sinton, 1981; Sinton et al., 1983; Fornari et al., 1983; Perfit and Fornari, 1983a, b) demonstrated, on the Galapagos spreading center and the Juan de Fuca ridge, that tips of PSC are a special class of ridge-transform intersection. They showed that the balance between cooling and supply rates of new magma batches into shallow reservoirs is conducive to the development of advanced degrees of differentiation over an expanded length of ridge. While significant variations of Fe concentration are often evident in basalts erupted at propagating spreading centers, the highest Fe content is not always found at the tip, but often at some distance behind it (Christie and Sinton, 1981; Sinton et al., 1983; Juteau et al., 1995).

Furthermore, some other workers (Nicolas, 1989; Gente et al., 1995) showed that segmentation along the ridge axis can reflect the activity of a mantle diapir beneath magma reservoirs. In particular, Nicolas (1989) and Ceuleneer and Rabinowicz (1992) indicated that one of the segments of the fossil ridge axis from the Oman ophiolite showed different lines of flow in mantle diapir, along and across the axis.

Despite these recent progress in understanding the segmentation of spreading centers and the behavior of PSCs, key questions still remain unanswered: i) Is there an asthenospheric diapir beneath a PSC? ii) If so, is the diapir focused beneath the center of PSC or elsewhere? iii) Is there magma transportation along the axis of a PSC? iv) Is there any difference of behavior of a PSC related to its geodynamic settings (*e.g.* mature oceanic basin *versus* back-arc basin)? This paper, focused on an example located in a mature back-arc basin, gives new insights into the origin and implications of the process of propagation of spreading axes.

## Geological setting

The North Fiji Basin is a  $\geq 12$  Ma old back-arc basin, located in the SW Pacific. Different reconstructions of the evolution of the North Fiji Basin (called NFB

hereafter) have been proposed over the last 25 years (*Chase, 1971; Gill and Gorton, 1973; Falvey, 1975; Dubois et al., 1977; Malahoff et al., 1982; Auzende et al., 1988a, b, 1995; Pelletier et al., 1993, 1999*). The latest ones have shown that the basin began to open around 12 Ma, after the Vitiaz subduction ceased in response to the collision of the large Ontong Java Plateau with the arc, causing a reversal of

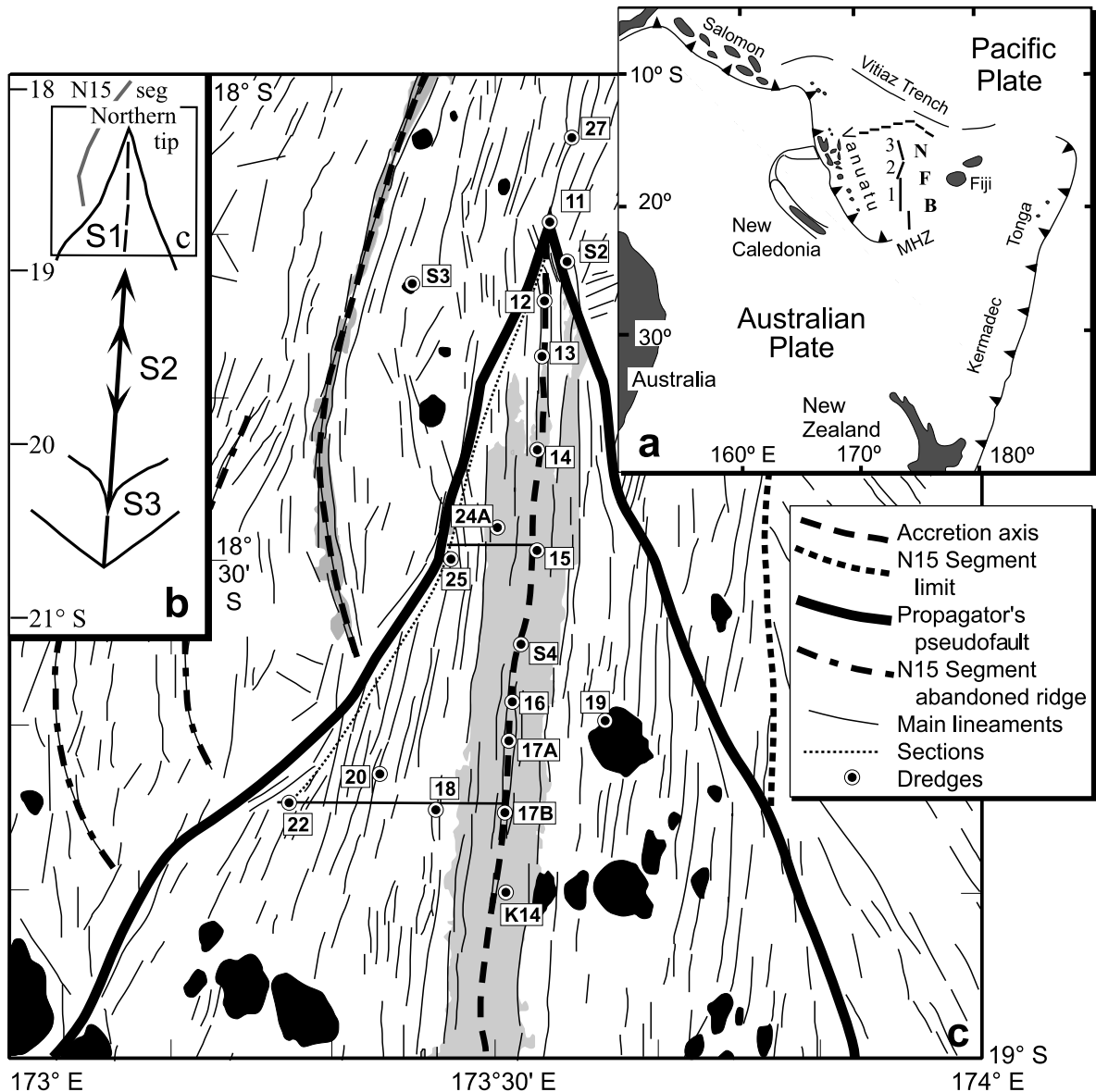


Fig. 1. Location of the study area: **a** general map of the North Fiji Basin (NFB); 1 = NS-propagating spreading center (NS-PSC); 2 = N15-segment; 3 = N160-segment; MHZ Matthew-Hunter Zone; **b** simplified axial segmentation S1, S2 and S3 of the NS-PSC; N15 seg = N15-segment; **c** simplified structural map of the segment S1 of the NS-PSC with the location of the dredges from the ProFeTi cruise (modified after *Ruellan et al., 1994*)

the subduction from the southwestward deeping Pacific slab along the Vitiaz trench to the northeastward deeping Australina slab along the New Hebrides trench. Thereafter, the NFB opened in a complex succession of stages until it reached its present configuration (Auzende et al., 1995). It is presently delimited by the New Hebrides island arc to the West, the Matthew-Hunter zone to the South, the Fiji platform to the East and the fossil Vitiaz subduction zone to the North (Fig. 1a). Between 15° S and 21° S, the active spreading system is divided into three main parts (Fig. 1): the N160-segment, N15-segment and the NS-propagating spreading center. The latter was emplaced 3 Ma ago over an older spreading system oriented N140. Previous work completed during the French-Japanese STARMER program revealed that the 280 km long NS-propagating spreading center (called NS-PSC hereafter) has been propagating northward at the expense of the N15-segment at a rate of 5.7 cm/yr. since at least 1 Ma (de Alteriis et al., 1993; Ruellan et al., 1994). The NS-PSC is limited to the North and to the South by two pairs of pseudofaults. The axis itself is divided into three sub-segments S1, S2 and S3 (about 110 km long) delineated by secondary offsets (Fig. 1b). These segments are themselves divided into smaller units (26 km long on average), separated by third order discontinuities.

In order to unravel the rock-forming processes of the NS-PSC in the NFB, extensive sampling was undertaken in 1994 during the ProFeTi cruise onboard *R/V Alis*. Dredges were evenly distributed with one dredge every 5 km along-axis and one dredge every 3 km across-axis, along two sections on the western side of the northern tip of the NS-PSC (Fig. 1c). This sampling allowed the detailed study of the geochemical signature of zero-age abyssal lavas collected along axis, and also for those collected across-axis between zero and 1 Ma (age deduced from magnetic data, Ruellan et al., 1994). Only the northern 67 km of the spreading center was sampled during the ProFeTi cruise, the rest of the axis having been sampled previously (Eissen et al., 1991, 1994; Nohara et al., 1994a, b).

### **Petrography and mineralogy**

Most of the sampled lavas have a glassy texture and contain few vesicles (0.01–1.4%; Table 1). They originate from two main kinds of effusive bodies: pillow-lavas (80%) or draped massive lava flows. These basalts present the typical mineralogy of MORB's with plagioclase, olivine, clinopyroxene and accessory spinel in decreasing order of abundance. Their modal content varies from aphyric to porphyritic (percentage of phenocrysts ranging from 0 to 25 vol.%; see Table 1). Representative minerals have been analyzed using the CAMEBAX SX50 electron microprobe at Brest (France). Some representative results and the analytical conditions are listed in Table 2.

#### *Olivine*

The olivine crystals are euhedral to sub-euhedral microphenocrysts to phenocrysts, with composition varying with their geographical position. Along the N15-segment, compositions vary between Fo<sub>77</sub> and Fo<sub>90</sub> with the more magnesian olivines

Table 1. *Provenance and description of the collected samples and brief summary of the mineralogical parageneses. Vol.% is the modal percentage of phenocrysts in each sample (optical estimation); Vesc.% is the modal percentage of vesicles estimated by image analysis counting after treatment (Launeau et al., 1998). Plagio plagioclase, Cpx clinopyroxene, microlite (<0.1 mm) not estimated,  $\mu$ p microphenocryst (0.1–0.5 mm), ph phenocryst (0.5–2 mm), M megacryst (>2 mm), VZ variolitic zone, BG basaltic glass*

Sample number	Sample texture	Mesostasis				Mineral types				Vol.%	Vesc.%
		Plagio	Olivine	Cpx	Spinel	Plagio	Olivine	Cpx	Spinel		
N–S PSC axis: PFT94-D11 (18°07.68′ S–173°32.65′ E: 2930 m)											
1A	basaltic glass					μp	μp	μp		25	
1B	variolic zone					μp	ph + μp	μp		20	
2	BG + VZ	+		+	+	+	ph	μp		20	1.35
N–S PSC axis: PFT94-D12 (18°12.74′ S–173°32.71′ E: 3030 m)											
1	BG + VZ	+		+		M + ph	ph	M		20	
1g	basaltic glass	+	+	+		ph + μp	ph			20	
2	BG + VZ	+	(+)	+			ph			20	0.54
2g	BG + VZ	+	+	+		M	ph	M + ph		20	
N–S PSC axis: PFT94-D13 (18°17.47′ S–173°32.01′ E: 3145 m)											
1	sheet flow					μp	μp			0.5	
2g	BG + VZ	+		+		μp	M + ph			0.5	0.54
N–S PSC axis: PFT94-D14 (18°10.05′ S–173°24.58′ E: 3055 m)											
1	basaltic glass					M + μp	μp	(μp)		2	
2	BG + VZ	+	(+)	+		M + μp	M + μp	μp		5	0.65
3	BG + VZ	+	+	(+)		μp	μp	μp		10	
4	BG + VZ	+	+			μp	μp			10	
N–S PSC axis: PFT94-D15 (18°28.18′ S–173°31.34′ E: 2920 m)											
1	BG + VZ	+	+	+		μp	ph + μp	ph + μp		10	
1g	basaltic glass					μp	μp	μp		<10	
2	basaltic glass	+	+	+		μp	μp	μp		10	0.60
2g	basaltic glass	+	+	+		μp	μp	μp		10	
N–S PSC axis: PFT94-D16 (18°38.43′ S–173°30.29′ E: 2765 m)											
1	fluidal + VZ	+	(+)			ph + μp	ph + μp			2	
1g	basaltic glass	+	+			μp	μp			3	0.51
2	BG + VZ	+	+			M + μp	μp			3	
2g	basaltic glass					M + μp	μp			1	
3	BG + VZ	+	+			M + μp	μp			3	
3g	basaltic glass					M + μp	μp			1	
4	basaltic glass	+	+			M + μp	μp			1	
N–S PSC axis: PFT94-D17A (18°40.34′ S–173°30.13′ E: 2785 m)											
1	BG + VZ	(+)	+			μp	μp	μp		10	0.11
1g	basaltic glass					μp	μp	μp		9	
N–S PSC axis: PFT94-D17B (18°44.37′ S–173°30.07′ E: 2740 m)											
1	BG + VZ	+	+			μp	μp			9	
1g	basaltic glass	+	+			μp	μp			9	

(continued)

Table 1 (*continued*)

Sample number	Sample texture	Mesostasis				Mineral types				Vol.%	Vesc.%	
		Plagio	Olivine	Cpx	Spinel	Plagio	Olivine	Cpx	Spinel			
N-S PSC axis: PFT94-D18 (18°43.57' S–173°25.69' E: 2845 m)												
1	BG + VZ	+	+			µp	ph + µp			4	0.53	
1g	basaltic glass	+	+			µp	ph + µp			4		
2	BG + VZ	+	+			µp	ph + µp			4		
3	variolitic zone	+	+			M + µp	M + µp		in oliv.	4		
N-S PSC axis: PFT94-D19 (18°40.21' S–173°36.62' E: 2550 m)												
1	BG + VZ	+	+			µp			µp	<1		
1g	fluidal + VZ	+	+			µp	µp			<1		
2	fluidal + VZ	+	+			µp	µp			<1		
N-S PSC axis: PFT94-D20 (18°42.02' S–173°22.47' E: 2960 m)												
1A	doleritic	+	+	+		µp	µp		µp	1	0.09	
1B	doleritic	+	+	+		µp	µp		µp	1		
1C	BG + VZ	+	+	+		µp	µp		µp	1		
1D	doleritic	+	+	+		µp	µp		µp	1		
1E	doleritic	+	(+)	+		ph + µp	(µp)		µp	6		
N-S PSC axis: PFT94-D22 (18°44.27' S–173°19.02' E: 2915 m)												
1	variolitic zone	+	(+)			µp	µp		µp	in oliv.	10	0.44
2	variolitic zone	+	(+)			ph + µp	µp		µp	in oliv.	10	
2g	basaltic glass	+	+			ph + µp	µp		µp	in oliv.	7	
N-S PSC axis: PFT9-D24A (18°26.93' S–173°29.88' E: 2875 m)												
1	variolitic zone										0	
1g	variolitic zone					ph					0.1	
1*	basaltic glass	+	+	(+)		ph			ph		0.2	
N-S PSC axis: PFT94-D25 (18°28.88' S–173°25.57' E: 2675 m)												
1	basaltic glass	+									0	0.72
1g	basaltic glass										0	
2	basaltic glass	+									0	
2g	basaltic glass	+									0	
3	doleritic	+	+			ph + µp	ph + µp				1	
4	doleritic	+	(+)	+		M					1	
5	basaltic glass					µp	µp		µp		2	
N-S PSC axis: PFT94-D27 (18°04.57' S–173°33.46' E: 2750 m)												
1	basaltic glass					µp	µp		µp		9	0.65
1g	basaltic glass					µp	µp		(µp)		9	
2	basaltic glass					µp	µp		µp		10	
2g	basaltic glass					µp	µp		(µp)		10	

found towards the southern tip of the segment and with some crystals having inverse zoning. Along the NS-PSC, on-axis compositions are between Fo<sub>66</sub> and Fo<sub>88</sub> with no systematic geographical variations. Olivines collected off-axis and

along the pseudo-fault are more magnesian and have a more restricted compositional range between Fo<sub>75</sub> and Fo<sub>88</sub> (Fig. 2a).

Olivine-liquid equilibrium (Roeder and Emslie, 1970) was investigated on a few selected samples. Along the NS-PSC, most of the results fit inside the range of equilibrium;  $0.29 < \text{apparent } K_d's < 0.36$  (Ulmer, 1989). Only a small proportion of olivine exhibits apparent  $K_d's < 0.29$  in disequilibrium with their present host glass. These crystals correspond to the most primitive olivine. Three generations of crystals are recognized along the N15-segment;

- 1) a late stage generation in disequilibrium ( $0.42 < \text{apparent } K_d's < 0.55$ ) corresponding presumably to late crystallization during the lava extrusion;
- 2) generation at equilibrium corresponding to crystallization within the magma chamber;
- 3) a generation in equilibrium with a more primitive liquid ( $0.25 < \text{apparent } K_d's < 0.29$ ) found only at the southernmost sampling site (K6; Eissen et al., 1991).

Using equations of olivine-liquid equilibrium (Roeder and Emslie, 1970; Ulmer, 1989), the temperature of extrusion of the magma was calculated on olivine phenocrysts at equilibrium with their host magma. The temperature decreases to the south along the N15-segment from 1200 to 1080 °C, and then increases at the contact of the NS-PSC up to 1180–1220 °C. Along the NS-PSC, temperature remains relatively uniform, *i.e.* higher compared with the N15-segment. Therefore, it seems that magmatic temperatures directly correlate with the magma reservoir behavior. Calculated temperatures on off-axis samples from the NS-PSC western pseudofault show that magma tapped at the tip is cooler since 1 Ma (1160–1200 °C). Few kilometers from the tip, the magma has only recently (0.3 Ma) been warmed-up.

#### *Glomerocrystal of evolved olivine*

Sample PFT94-D14-2 collected at 25 km from the propagator tip along the NS-PSC contains a 5 × 3 mm olivine + plagioclase + clinopyroxene + spinel + glass glomerocrystal. Its texture is similar to a gabbroic heteradcumulate, an olivine megacryst enclosing the other phenocrysts. Olivine oscillatory zoning (Fo<sub>71</sub> > Fo<sub>69</sub> > Fo<sub>75</sub>) is first in the range of equilibrium with the host glass, then becomes too mafic (Fig. 2b). Clinopyroxenes are the most iron-rich of this area (~Fs<sub>30–40</sub>; Table 2). This glomerocryst presumably corresponds to a gabbroic xenolith, pulled away from the crystallization zone at the top of the magma chamber during magma extraction as described in other PSC (Eaby-Dixon et al., 1986).

#### *Clinopyroxene*

Clinopyroxenes are found as euhedral to sub-euhedral microphenocrysts to phenocrysts, associated most frequently in clusters with plagioclase and olivine. Along the NS-PSC they are more abundant on the last segment just before the propagating tip. Clinopyroxenes are compositionally quite homogeneous (Fig. 2c) with no correlation of composition with crystal size. Partition coefficients (Ulmer, 1989)



Table 2. Selected compositions of clinopyroxene, olivine and plagioclase from the North Fiji Basin Propagating Spreading Center. Analytical conditions: accelerating voltage = 15 kV; beam current = 20 nA; spot beam of 1  $\mu$ m; analysts: C. Fleutelot and M. Bohn. A complementary dataset is available upon request from the corresponding author

Clinopyroxene											
Sample	D11-1A	D11-1A	D14-2	D17A-1g	D17A-1g	D20-1C	D20-1C	D25-5	D27-1	D27-1	D27-1
Size (µm)	100	100	20	200	200	300	300	120	150	150	120
Core/Rim	core	rim	core	core	core	rim	core	core	core	core	rim
SiO <sub>2</sub>	50.51	50.28	47.53	51.03	51.13	53.20	50.72	51.56	51.92	51.92	50.28
TiO <sub>2</sub>	0.82	0.92	1.90	0.88	0.62	0.32	0.73	0.67	0.78	0.78	1.16
Al <sub>2</sub> O <sub>3</sub>	3.14	2.99	7.77	3.84	3.15	1.57	3.74	2.11	2.76	2.76	4.07
Fe <sub>2</sub> O <sub>3</sub>	3.72	3.87	2.56	2.22	3.15	2.69	3.58	2.83	1.73	1.73	2.16
FeO	5.48	6.58	15.25	6.19	3.77	6.09	4.69	7.36	7.17	7.17	6.60
MgO	18.08	16.70	12.33	18.09	17.88	21.68	18.34	16.34	17.50	17.50	15.95
Cr <sub>2</sub> O <sub>3</sub>	0.28	0.12	0.10	0.49	0.50	0.21	0.19	0.14	0.23	0.23	0.38
MnO	0.19	0.31	0.28	0.11	0.22	0.21	0.26	0.16	0.31	0.31	0.29
NiO	0.00	0.00	0.06	0.07	0.01	0.22	0.03	0.00	0.00	0.00	0.00
CaO	17.05	17.72	11.14	17.25	19.60	13.93	17.35	18.63	17.46	17.46	19.20
Na <sub>2</sub> O	0.28	0.33	1.43	0.23	0.15	0.19	0.29	0.34	0.29	0.29	0.26
K <sub>2</sub> O	0.02	0.00	0.00	0.00	0.00	0.00	0.00	0.03	0.12	0.12	0.00
Total	99.56	99.81	100.33	100.40	100.17	100.30	99.93	100.17	100.26	100.26	100.35
Si	1.864	1.866	1.790	1.864	1.870	1.925	1.858	1.908	1.905	1.905	1.854
Al <sup>iv</sup>	0.136	0.131	0.210	0.136	0.130	0.067	0.142	0.092	0.095	0.095	0.146
Al <sup>vi</sup>	0.001	0.000	0.135	0.029	0.006	0.000	0.020	0.000	0.025	0.025	0.031
Ti	0.023	0.026	0.054	0.024	0.017	0.009	0.020	0.019	0.021	0.021	0.032
Fe <sup>3+</sup>	0.102	0.106	0.070	0.060	0.086	0.072	0.098	0.077	0.047	0.047	0.059
Cr	0.008	0.004	0.003	0.014	0.014	0.006	0.005	0.004	0.007	0.007	0.011
Mg	0.994	0.924	0.692	0.985	0.975	1.169	1.002	0.901	0.957	0.957	0.877
Ni	0.000	0.000	0.002	0.002	0.000	0.006	0.001	0.000	0.000	0.000	0.000
Fe <sup>2+</sup>	0.171	0.206	0.483	0.190	0.116	0.185	0.145	0.229	0.221	0.221	0.205
Mn	0.006	0.010	0.009	0.003	0.007	0.006	0.008	0.005	0.010	0.010	0.009
Ca	0.674	0.705	0.449	0.675	0.768	0.540	0.681	0.739	0.686	0.686	0.759
Na	0.020	0.024	0.104	0.016	0.010	0.013	0.021	0.024	0.021	0.021	0.019
K	0.001	0.000	0.000	0.000	0.000	0.000	0.000	0.002	0.006	0.006	0.000
Sum cations	4.000	4.000	4.000	4.000	4.000	4.000	4.000	4.000	4.000	4.000	4.000

Continued

(continued)

Table 2 (continued)

Petrogenetic variability along the NS-PSC											63
Clinopyroxene											
Wo %	36.7	38.4	27.7	36.5	41.3	28.5	37.3	39.5	36.8	41.2	
En %	54.1	50.4	42.6	53.2	52.4	61.7	54.8	48.2	51.3	47.7	
Fs %	9.3	11.2	29.7	10.3	6.2	9.8	7.9	12.3	11.8	11.1	
Olivine											
Plagioclase											
Sample	D27-1	D27-2g	D14-3	D14-3	D17B	D17B	D18-1g	D20-1E	Sample	D12-2g	D19-2
Size (µm)	150	150	250	250	400	400	200	200	Size (µm)	80	200
Core/Rim	core	rim	core	core	rim	core	core	rim	Core/Rim	rim	core
SiO <sub>2</sub>	39.73	39.00	39.32	38.94	39.40	39.06	39.09	39.65	SiO <sub>2</sub>	51.74	47.05
TiO <sub>2</sub>	0.00	0.10	0.03	0.03	0.10	0.04	0.03	0.00	TiO <sub>2</sub>	0.06	0.06
Al <sub>2</sub> O <sub>3</sub>	0.04	0.07	0.03	0.04	0.09	0.09	0.02	0.06	Al <sub>2</sub> O <sub>3</sub>	29.73	33.29
FeO	19.94	19.85	14.39	14.81	15.55	15.05	18.92	15.12	Fe <sub>2</sub> O <sub>3</sub>	0.86	0.49
MgO	41.11	40.18	45.11	45.15	43.99	44.34	41.70	44.70	MgO	0.24	0.20
MnO	0.34	0.40	0.16	0.41	0.17	0.22	0.40	0.24	CaO	13.49	17.34
CaO	0.31	0.37	0.30	0.29	0.29	0.32	0.36	0.34	Na <sub>2</sub> O	4.19	1.87
Cr <sub>2</sub> O <sub>3</sub>	0.00	0.08	0.00	0.00	0.02	0.05	0.00	0.07			
NiO	0.12	0.00	0.18	0.20	0.35	0.23	0.02	0.00			
Total	100.54	100.05	99.53	99.87	99.97	99.40	100.54	100.17	Total	100.31	100.30
Si	0.991	1.003	0.992	0.983	0.995	0.990	0.996	0.995	Si	2.352	2.160
Al	0.000	0.002	0.001	0.001	0.003	0.003	0.001	0.002	Al	1.593	1.801
Ti	0.000	0.002	0.001	0.001	0.002	0.001	0.000	0.000	Ti	0.002	0.002
Fe <sup>2+</sup>	0.427	0.427	0.304	0.313	0.328	0.319	0.403	0.318	Fe <sup>3+</sup>	0.029	0.017
Mg	1.570	1.540	1.695	1.698	1.655	1.675	1.584	1.673	Mg	0.016	0.013
Mn	0.007	0.009	0.003	0.009	0.004	0.005	0.009	0.005	Na	0.369	0.166
Ca	0.008	0.010	0.008	0.008	0.008	0.009	0.010	0.009	Ca	0.657	0.853
Cr	0.000	0.002	0.000	0.000	0.000	0.001	0.000	0.001			
Ni	0.003	0.000	0.004	0.004	0.007	0.005	0.000	0.000			
Sum cations	3.008	2.994	3.007	3.016	3.002	3.007	3.003	3.003	Sum cations	5.019	5.012
Fo %	77.6	77.0	83.9	83.4	82.6	83.0	78.5	83.0	An %	64.0	83.7
Fa %	21.2	21.5	15.1	15.4	16.5	15.9	20.1	15.8	Ab %	36.0	16.3

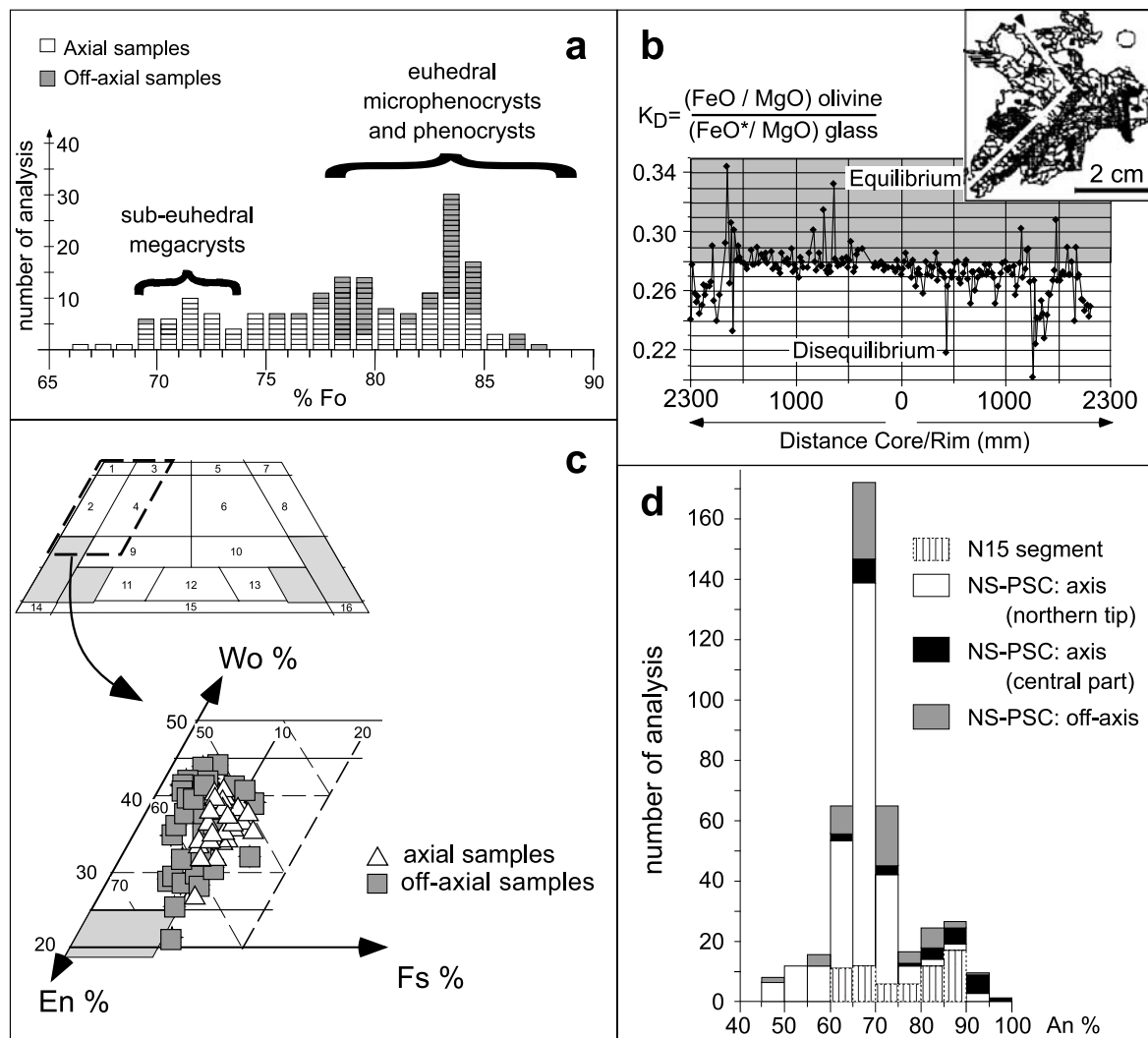


Fig. 2. Composition of the minerals: **a** olivine; **b** glomerocrystal of evolved olivine; **c** clinopyroxene; **d** plagioclase

calculated for the clinopyroxene-liquid equilibrium show that they crystallized in equilibrium with their host glass, both on- and off-axis. The only exceptions are for the pyroxene closest to the propagator tip, which are in slight disequilibrium and for the pyroxenes in sample PFT94-D14-2 which crystallized in a more evolved liquid as did the glomerocrystal included in this sample (see previous paragraph). The along-strike variations of the apparent  $K_d$ 's show a decrease towards the propagator tip. Using the  $\text{Ti}/\text{Al}^{\text{IV}}$  ratio as a geobarometer (*Thy, 1991*), the calculated pressures seem to be lower from 3 Ma ago than on the present axis and lower from the center of the PSC than towards to propagator tip. Clinopyroxenes from the N15-segment crystallized in a slightly more evolved magma (apparent  $K_d > 0.23$ ) and at a slightly lower temperature and pressure than observed along the NS-PSC.

### *Plagioclase*

Plagioclase is the most common mineral phase, being present from microlites to euhedral phenocrysts to megacrysts. They are generally chemically homogeneous, but the larger phenocrysts frequently show a small normal zoning towards their external rim (over the last 500  $\mu\text{m}$ ), grown at the same time as the microphenocrysts and the microlites. Calculations of  $K_d$ 's (Drake and Weill, 1975; Grove and Bryan, 1983) show that most of the phenocrysts crystallized in equilibrium with their host magma except for the zoned external rims. The microphenocrysts and the microlites crystallized from more evolved liquids compared with the core of large phenocrysts from the northern tip of segment S1 and N15-segment which crystallized from more primitive liquids (Fig. 2d).

### *Spinel*

Spinel consists mainly of very small size (diameter = 5–10  $\mu\text{m}$ ) titanomagnetite in the mesostasis or small titanomagnetite laths ( $5 \times 50 \mu\text{m}$ ) and small ilmenite grains (diameter  $\sim 10 \mu\text{m}$ ) in the segregation vesicles of the MORB's and Fe–Ti basalts. None of them crystallized as phenocrysts in the magma.

### *Alteration, maghemitization*

Low-temperature alteration is marked by palagonitization and Fe–Mn coating of the external glass rim, and by vesicles filled with secondary minerals (celadonite, iron-oxihydroxides, etc) as samples are located farther from the axis. Sample PFT94-D18-3 shows zeolites (thomsonite-type) filling in a few small vesicles, indicating a higher temperature ( $>100^\circ\text{C}$ ) alteration by fluids derived from hydrothermal circulation (Manac'h, 1997).

The joint analysis of magnetic and geochemical properties of the basalts collected along and across-axis of the NS-PSC suggests that two effects control the variations of the natural remanent magnetization (NRM): i) extensive magma differentiation up to Fe–Ti basalts increases with the intensity of NRM and both increase towards the NS-PSC northern tip; ii) low-temperature oxidation (maghemitization) seems to be already effective along the ridge axis for the zero age basalts (Horen and Fleutelot, 1998).

## **Geochemistry**

### *Analytical procedure*

#### ICP-AES

47 samples, finely powdered in an agate mill, were analyzed in Brest (UMR 6538). To obtain a clear solution of 100 ml, 300 mg of sample were digested at  $80^\circ\text{C}$  with 4 ml of a concentrated acid mixture ( $\text{HF}$ ,  $\text{HNO}_3$ ) in a 30 ml screw cap PFA bottle and then 96 ml of an  $\text{H}_3\text{BO}_3$  solution was added to dissolve the precipitate fluoride and neutralize the excess  $\text{HF}$ . Major and trace elements were measured by

Table 3. Selected bulk rock geochemical analysis from the North Fiji Basin Propagating Spreading Center. For the full sample number, refer to Table 1.  $Fe_2O_3^*$  = total iron given as  $Fe_2O_3$  for ICP-AES analyses. Trace elements: numbers given in *italics* refer to ICP-MS analyses, the others refer to ICP-AES analyses. LOD limit of detection. Concentrations measured by ICP-AES and ICP-MS are in good agreement: analytical comparisons between element concentration measured by ICP-AES and ICP-MS show correlation coefficients up to 0.97. Operating parameters for ICP-AES are described in Cotten et al. (1995). All lead isotopic results are an average of 2 independent analyses of 2 different aliquots of the same powder. A complementary dataset of 24 analysis is available upon request from the corresponding author J. P. Eissen

Sample	D11-1A	D12-1	D12-2g	D13-2g	D14-1	D14-2	D15-1g	D16-1g	D17A-1g	D17B-1g	D18-2
<i>Major elements (wt.%)</i>											
SiO <sub>2</sub>	49.80	50.00	50.30	49.30	50.20	49.50	50.50	50.30	50.50	50.10	49.90
TiO <sub>2</sub>	2.32	1.97	1.99	2.02	1.26	2.31	1.72	1.24	1.61	1.29	1.80
Al <sub>2</sub> O <sub>3</sub>	12.90	13.50	13.50	13.39	14.85	12.94	13.50	15.15	13.85	14.63	13.78
Fe <sub>2</sub> O <sub>3</sub> *	15.45	14.44	14.45	14.56	11.60	15.60	13.75	11.40	12.62	11.82	13.40
MnO	0.24	0.25	0.23	0.40	0.19	0.24	0.22	0.19	0.21	0.19	0.21
MgO	6.00	6.71	6.80	6.73	8.28	6.22	6.95	8.02	7.33	8.02	6.95
CaO	10.30	10.85	11.00	10.79	12.00	10.30	11.16	12.14	11.60	12.00	11.15
Na <sub>2</sub> O	2.55	2.49	2.45	2.40	2.20	2.54	2.47	2.36	2.34	2.22	2.49
K <sub>2</sub> O	0.14	0.11	0.09	0.13	0.06	0.14	0.10	0.07	0.09	0.06	0.13
P <sub>2</sub> O <sub>5</sub>	0.23	0.19	0.19	0.22	0.13	0.22	0.17	0.13	0.16	0.13	0.18
LOI	-0.69	-0.51	-0.85	-0.24	-0.87	-0.60	-0.91	-0.86	-0.45	-0.90	-0.50
Total	99.24	100.00	100.15	99.70	99.90	99.41	99.63	100.14	99.86	99.55	99.49
<i>Trace and rare earth elements (ppm)</i>											
Rb	2.3	1.5	1.3	1.75	1	1.6	1.9	1.3	1.9	0.7	1.3
Rb		1.11		1.48	0.86		1.97	1.09	1.8	0.82	
Sr	85	75	72	100	78	84	82	84	81	68.5	92
Sr		71.7		99.35	75.3		82.1	84.1	82.4	71.3	
Cs		0.03		0.0225	0.02		0.05	0.02	0.04	0.02	
Ba	17	11.2	8.5	31	7.5	13	10	9	10.5	6.5	13
Ba		11.9		30.85	8.3		10.8	10.1	12	7.5	
Sc	44	44	45	43.5	41.5	45	44	41.5	43	39.5	41
V	450	432	435	432	330	477	400	313	375	327.5	380
Cr	65	102	101	172	300	86	122	275	250	285	150
Co	46	47	46	51	46	47	47	44	45	45.5	45
Ni	49	60	58	75	111	55	64	98	72	99	65
Y	58	49	48	51	31	55	42	30	39	32	43
Y		46.8		49.6	30.5		42.8	30.8	40	32.8	
Zr	148	112	112	128	70	140	98	68	95	68.5	106
Zr		115.8		134.65	72.8		108.9	73.3	104.3	76.2	
Nb	4.2	2.65	2.5	3.3	1.85	3.5	2.35	1.7	2.3	1.775	2.9
Nb		1.8		2.6	1.3		1.8	1.4	1.9	1.4	
Hf		3.2		3.45	1.98		2.7	1.83	2.56	1.94	

(continued)

Table 3 (continued)

Sample	D11-1A	D12-1	D12-2g	D13-2g	D14-1	D14-2	D15-1g	D16-1g	D17A-1g	D17B-1g	D18-2
Ta		0.14		0.17	0.09		0.12	0.15	0.13	0.1	
Pb		1.27		4.505	0.54		0.79	0.64	0.98	0.71	
Th		0.16		0.26	0.15		0.58	0.2	0.47	0.12	
U		0.1		0.165	0.05		0.09	0.05	0.11	0.04	
La	5.3	3.8	3.6	6.3	2.5	4.65	3.6	2.6	3.4	2.3	3.95
La		3.56		6.05	2.34		3.21	2.35	3.33	2.25	
Ce	18	12.6	13.3	16.5	9	16	12	8.5	11.5	8	13.5
Ce		11.36		15.685	7.56		10.49	7.24	10.18	7.33	
Pr		2.06		2.675	1.33		1.84	1.29	1.81	1.31	
Nd	16	13.1	12.3	14	8	15	11	7	10	7.25	11
Nd		11.99		14.63	7.73		10.74	7.36	10.32	7.73	
Sm		4.32		4.865	2.82		3.73	2.61	3.55	2.77	
Eu	1.8	1.5	1.5	1.65	1.05	1.6	1.38	1.05	1.25	1.075	1.43
Eu		1.53		1.63	1.04		1.36	1.03	1.29	1.04	
Gd		6.39		6.88	4.12		5.5	3.94	5.14	4.16	
Tb		1.16		1.215	0.75		1.01	0.71	0.93	0.76	
Dy	9.5	8.2	8.2	8.5	5.3	9.2	7.1	5.1	6.6	5.45	7.2
Dy		8.04		8.325	5.25		6.98	5.03	6.52	5.32	
Ho		1.75		1.815	1.14		1.52	1.1	1.41	1.16	
Er	5.8	5	5	5.3	3.2	5.7	4.3	3.2	4	3.2	4.3
Er		5.14		5.33	3.35		4.37	3.13	4.08	3.36	
Tm		0.749		0.7775	0.485		0.659	0.476	0.61	0.505	
Yb	5.8	5	4.975	5.22	3.225	5.7	4.16	3.1	4.05	3.313	4.375
Yb		4.86		5.06	3.15		4.16	2.95	3.84	3.18	
Lu		0.778		0.8105	0.511		0.667	0.476	0.622	0.516	
<i>Isotopic ratios</i>											
<sup>206</sup> Pb/ <sup>204</sup> Pb	18.138		18.109	18.485	18.060	18.093	18.213	18.214	18.119	18.063	18.224
<sup>207</sup> Pb/ <sup>204</sup> Pb	15.505		15.493	15.569	15.500	15.494	15.506	15.506	15.513	15.468	15.517
<sup>208</sup> Pb/ <sup>204</sup> Pb	37.899		37.850	38.359	37.810	37.874	37.987	37.979	37.983	37.750	38.992
<sup>143</sup> Nd/ <sup>144</sup> Nd	0.513097		0.513111	0.513089	0.513125	0.513108	0.513094	0.513078	0.513127	0.513128	0.513071
<sup>87</sup> Sr/ <sup>86</sup> Sr	0.702976		0.702869	0.703015	0.702886	0.702920	0.702941	0.703027	0.702872	0.702863	0.703086
Sample	D19-1g	D20-1A	D20-1E	D22-2g	D24A-1g	D25-1g	D25-3	D27-1g	BIR-1	std-dev	LOD (ppm)
<i>Major elements (wt.%)</i>											
SiO <sub>2</sub>	50.00	49.80	50.20	49.50	50.00	49.60	49.70	49.50			
TiO <sub>2</sub>	1.26	1.51	1.20	1.17	2.40	1.55	1.52	1.87			
Al <sub>2</sub> O <sub>3</sub>	15.05	14.00	14.60	15.28	13.05	14.40	15.50	13.80			
Fe <sub>2</sub> O <sub>3</sub> *	11.45	12.90	11.42	11.18	15.90	12.40	11.00	13.38			

(continued)

Table 3 (continued)

Sample	D19-1g	D20-1A	D20-1E	D22-2g	D24A-1g	D25-1g	D25-3	D27-1g	BIR-1	std-dev	LOD (ppm)
MnO	0.19	0.22	0.20	0.19	0.25	0.20	0.18	0.25			
MgO	8.20	6.96	7.78	8.23	6.00	7.40	7.70	6.72			
CaO	12.35	11.46	12.38	12.07	10.20	11.70	11.65	10.80			
Na <sub>2</sub> O	2.27	2.37	2.50	2.31	2.70	2.52	2.54	2.70			
K <sub>2</sub> O	0.04	0.24	0.07	0.08	0.13	0.14	0.26	0.23			
P <sub>2</sub> O <sub>5</sub>	0.11	0.15	0.11	0.11	0.24	0.16	0.19	0.23			
LOI	-0.89	0.27	-0.49	-0.42	-1.01	0.22	-0.05	0.09			
Total	100.03	99.88	99.87	99.70	99.86	99.85	100.19	99.57			
<i>Trace and rare earth elements (ppm)</i>											
Rb	0.8	5.2	1.4	1.3	2.2	2.2	3.4	3			0.5
Rb	0.65	4.72		0.92	1.58	1.87	2.83	3.11	0.22	±0.01	0.03
Sr	47	85	88	81	83	100	130	130			1.0
Sr	44.8	82.5		79	81.2	100.3	132.3	134.9	106	±2	6
Cs	0.02	0.3		0.03	0.02	0.04	0.06	0.05			
Ba	4.5	10	5	7	16	18.5	25	31	6.5	±0.2	3.0
Ba	5.3	10.9		8.2	16.1	18.4	24.8	30.3			0.6
Sc	40	44	45	42	44	42	38	42			0.5
V	315	370	303	287	470	338	305	354			3.0
Cr	372	120	240	360	60	220	315	160			3.0
Co	45	46	44	45	46	44	43	44			1.5
Ni	104	62	63	110	46	75	117	66			3.0
Y	34	38	30	29.4	59	36	33	44			1.0
Y	32.3	36.6		27.5	56.2	35.6	31.4	42.2	15.5	±0.3	0.9
Zr	63	84	61	61	155	91	98	133			3.0
Zr	64.9	87.5		63.4	157.8	97.9	102.3	141.9	13.7	±0.3	0.9
Nb	1.4	2.05	1	1.1	3.8	3.1	4.6	4.3			0.5
Nb	1	1.5		0.8	3	2.75	3.8	3.7	0.56	±0.6	1.8
Hf	1.93	2.36		1.77	4.21	2.4	2.56	3.29	0.579	±0.009	0.03
Ta	0.08	0.24		0.11	0.22	0.2	0.25	0.25	0.043	±0.007	0.02
Pb	0.43	0.82		0.78	0.87	1.07	0.7	2.72	3.05	±0.01	0.03
Th	0.11	0.14		0.07	0.27	0.23	0.39	0.32	0.031	±0.002	0.01
U	0.04	0.15		0.03	0.09	0.08	0.15	0.14	0.01	±0.001	0.01
La	1.85	2.85	1.9	1.8	5.15	3.7	4.9	6.1			0.5
La	1.77	2.67		1.78	4.9	3.59	4.48	5.85	0.68	±0.2	0.6
Ce	7	10	7.3	6.5	17.2	12	14.6	17.5			2.0
Ce	5.93	8.76		6.03	15.79	10.69	12.79	15.78	1.94	±0.5	1.5
Pr	1.14	1.54		1.12	2.71	1.79	2.02	2.62	0.381	±0.008	0.02
Nd	6.6	9	6.5	6.2	15.8	10	11	15.4			2.0
Nd	6.97	8.96		6.72	15.64	9.88	10.69	14.1	2.42	±0.05	0.15
Sm	2.76	3.24		2.45	5.34	3.36	3.46	4.34	1.08	±0.02	0.06

(continued)

Table 3 (continued)

Sample	D19-1g	D20-1A	D20-1E	D22-2g	D24A-1g	D25-1g	D25-3	D27-1g	BIR-1	std-dev	LOD (ppm)
Eu	1.05	1.23	1.07	1.1	1.81	1.23	1.28	1.6			0.15
Eu	1.02	1.19		0.96	1.81	1.25	1.25	1.53	0.52	±0.06	0.02
Gd	4.26	4.76		3.71	7.66	4.85	4.6	6.02	1.85	±0.02	0.06
Tb	0.78	0.87		0.66	1.36	0.86	0.79	1.03	0.353	±0.002	0.01
Dy	5.5	6.3	5	4.6	9.6	6	5.5	7.2			0.03
Dy	5.48	6.07		4.6	9.31	5.97	5.39	6.93	2.56	±0.03	0.09
Ho	1.19	1.32		1.02	2.04	1.3	1.15	1.5	0.57	±0.004	0.01
Er	3.4	3.9	3	3	6	3.6	3.3	4.5			0.6
Er	3.5	3.9		2.93	5.99	3.7	3.24	4.39	1.68	±0.01	0.03
Tm	0.506	0.576		0.435	0.884	0.555	0.479	0.635	0.246	±0.003	0.009
Yb	3.5	3.85	3.05	2.925	5.925	3.6	3.25	4.375			0.1
Yb	3.26	3.69		2.77	5.65	3.46	3.1	4.07	1.61	±0.02	0.06
Lu	0.528	0.6		0.444	0.916	0.554	0.487	0.648	0.258	±0.003	0.009
<i>Isotopic ratios</i>											
$^{206}\text{Pb}/^{204}\text{Pb}$	18.109	18.223	18.121	18.260	18.119	18.278	18.215	18.375			
$^{207}\text{Pb}/^{204}\text{Pb}$	15.494	15.489	15.497	15.524	15.481	15.530	15.529	15.547			
$^{208}\text{Pb}/^{204}\text{Pb}$	37.864	38.012	37.856	38.056	37.826	38.104	38.057	38.213			
$^{143}\text{Nd}/^{144}\text{Nd}$	0.513130	0.513094	0.513135	0.513108	0.513109	0.513105	0.513068	0.513100			
$^{87}\text{Sr}/^{86}\text{Sr}$	0.702903	0.702906	0.702884	0.702962	0.702908	0.702996	0.703111	0.703005			



inductively coupled plasma atomic emission spectrometry (ISA Jobin-Yvon JY 70 PLUS), except Rb which was analyzed by flame atomic emission spectrometry (Perkin-Elmer 5000). For operating conditions see *Cotten et al. (1995)*. Calibrations were made using our own reference samples and controlled with international standard materials (BE-N, PM-S, JB-2). Relative standard deviations were  $\sim 1\%$  for  $\text{SiO}_2$  and  $\sim 2\%$  for the other major elements except MnO and  $\text{P}_2\text{O}_5$  ( $\pm 0.01\%$ ) and  $\text{K}_2\text{O}$  ( $\pm 0.005\%$ ) and  $\leq 5\%$  for trace elements. The limits of detection are calculated on the basis of three times the standard deviations for low trace element content and are given in Table 3.

### ICP-MS

ICP-MS trace element analyses were performed on 19 samples at the University of Montpellier using a PQ2+ TURBO mass-spectrometer of VGElemental. Operating parameters are: RF forward power = 1.350 kW; RF reflected power = 5 W; coolant argon flow rate = 13.5 l/min; auxiliary argon flow rate = 0.5 l/min; Meinhardt nebuliser argon flow rate = 0.900 l/min; spray chamber = double pass, water cooled ( $2^\circ\text{C}$ ). ICP-MS data acquisition: ions lens setting: optimized on  $^{115}\text{In}$ ; typical sensitivity =  $3 \cdot 10^7$  counts/s/mg  $\cdot \text{g}^{-1}$ ; detection mode = pulse counting; acquisition mode: peak jumping; dwell time: 10.24 to 40.98 ms (depending on isotopic abundances); 3 repeated integrations of 40 s each. Detection limits are calculated on the basis of three times the standard deviations for low concentration (BIR-1).

Sample preparation: 100 mg of sample were digested in a mixture of HF and  $\text{HClO}_4$  for 24 hours. Following evaporation on a heating table, 3 successive additions of  $\text{HClO}_4$  and evaporation cycles eliminate the residual HF. The dry residue was then mixed with a solution of  $\text{HNO}_3$  at 20 g with water and stored in a polycarbonate tube. A dilution of 2 to 10 achieve the preparation of the solution which was injected in the plasma at a 1‰ final dilution. This treatment did not dissolve all the refractory minerals but all the solutions obtained were limpid and without any precipitate.

Data acquisition: All the elements were determined by external calibration. Multielement standards were prepared with a separation of LREE and HREE. Interferences were low, of the order of 1% for Gd ( $^{157}\text{Gd}^+$  interfere with  $\text{CeOH}^+$  and  $\text{PrO}^+$ ) and for Yb ( $^{173}\text{Yb}^+$  interfere with  $\text{GdO}^+$ ). Nb and Ta were stabilized in the solution by HF. In order to minimize memory effects, Nb and Ta standards were prepared the day of their use without HF addition. Indium and Bi were used as internal standards. Results obtained on simultaneously analyzed international standard BIR-1 are also given in Table 3 and show good agreement with the compiled values (*Govindaraju, 1994*).

### Electron microprobe

Major element microprobe analyses (Table 4) were performed on 31 fresh glass rims with a CAMECA SX50 microprobe at Hobart (Tasmania). Each reported analysis is the average of at least four separate points of homogeneous composition.

Table 4. Selected glass rim analyses performed on the CAMECA SX50 electron microprobe at the University of Tasmania, Hobart, Australia (analyst: L. Danyushevsky). Analytical conditions; accelerating voltage = 15 kV; beam current = 20 nA; beam defocused to a spot of  $10 \times 8 \mu\text{m}$ .  $\text{FeO}^*$  = total iron given as  $\text{FeO}$ .  $\text{H}_2\text{O}$  was determined by Fourier transform infrared spectroscopy on the same glass chip (Danyushevsky et al., 1993). A complementary dataset of 14 analyses is available upon request from the corresponding author J. P. Eissen

Sample	D11-1A	D12-1g	D13-1	D14-1A	D14-2	D15-1g	D16-1g	D17A-1g	D17B-1g	D18-1	D19-1g	D20-1g	D22-1g	D24A-1g	D25-1g	D27-1
$\text{SiO}_2$	50.00	49.66	50.05	50.56	49.92	49.68	49.30	49.70	50.13	49.55	49.85	49.59	49.80	49.56	49.56	49.62
$\text{TiO}_2$	2.63	2.18	2.03	1.32	2.40	1.82	1.24	1.74	1.35	1.87	1.27	1.55	1.25	2.32	1.56	2.18
$\text{Al}_2\text{O}_3$	12.70	13.01	13.65	14.55	13.05	13.44	14.78	13.90	14.66	13.81	14.93	13.84	14.94	13.01	14.47	13.59
$\text{FeO}^*$	15.03	13.78	12.89	10.78	14.48	12.81	10.52	11.81	10.80	12.32	10.46	12.09	10.71	14.35	11.01	12.93
$\text{MnO}$	0.24	0.23	0.21	0.20	0.21	0.24	0.19	0.16	0.17	0.17	0.19	0.20	0.21	0.21	0.13	0.21
$\text{MgO}$	5.47	6.09	6.48	7.56	5.91	6.45	7.94	7.13	7.79	6.51	7.87	7.10	7.87	5.88	7.29	5.98
$\text{CaO}$	9.99	10.66	11.12	12.27	10.25	11.21	12.43	11.75	12.15	11.24	12.30	11.57	12.58	10.20	11.68	10.75
$\text{Na}_2\text{O}$	2.69	2.57	2.43	2.16	2.52	2.53	2.15	2.34	2.17	2.60	2.28	2.36	2.24	2.62	2.41	2.86
$\text{K}_2\text{O}$	0.13	0.08	0.09	0.05	0.11	0.07	0.04	0.06	0.05	0.11	0.06	0.06	0.04	0.12	0.09	0.18
$\text{P}_2\text{O}_5$	0.26	0.13	0.15	0.08	0.21	0.11	0.06	0.14	0.08	0.14	0.06	0.08	0.07	0.20	0.14	0.20
$\text{Cr}_2\text{O}_3$	0.03	0.01	0.03	0.05	0.03	0.04	0.06	0.04	0.04	0.04	0.05	0.03	0.01	0.01	0.03	0.01
$\text{H}_2\text{O}$	0.39	0.26	0.29	0.16	0.37	0.22	0.12	0.22	0.14	0.29	0.14	0.21	0.12	0.36	0.24	0.40
Total	99.56	98.66	99.42	99.74	99.46	98.62	98.83	98.99	99.53	98.65	99.46	98.68	99.84	98.84	98.61	98.91

Analytical comparisons of element concentrations measured by ICP-AES on whole rocks (glassy or not) and electron microprobe on glasses show correlation coefficients close to 1, with variations within the range of the analytical uncertainty (between 1 and 5%).

### Isotopic measurements

Basalts and glasses were crushed in an agate mortar after cleaning with ultrapure water. All samples (powder) were systematically leached with 0.1 N HCl for 10 min in an ultrasonic bath and carefully rinsed with ultrapure water to eliminate seawater or alteration contributions. Separations of Pb, Sr and Nd were performed on the same aliquot in Brest according to the procedure described in Dosso et al. (1991). Sr and Nd ratios were measured in dynamic mode. The correction values used for mass fractionation are 8.3752 for  $^{87}\text{Sr}/^{86}\text{Sr}$  and 0.721903 for  $^{146}\text{Nd}/^{144}\text{Nd}$ . The average values for the standards are NBS 987:  $0.71026 \pm 3$  ( $n=68$ ) and LA JOLLA:  $0.511852 \pm 10$  ( $n=34$ ). Pb isotope data were corrected to the values given in Todt et al. (1984) with a fractionation factor of 0.0011 per mass unit. The average values for the Pb isotope standard were  $16.908 \pm 3$ ,  $15.451 \pm 4$ ,  $36.579 \pm 15$  ( $n=34$ ) for  $^{206}\text{Pb}/^{204}\text{Pb}$ ,  $^{207}\text{Pb}/^{204}\text{Pb}$ ,  $^{208}\text{Pb}/^{204}\text{Pb}$ , respectively.

### Geochemical results

#### Major elements and volatiles

Samples from the NS-PSC and those from the N15-segment have a homogeneous basaltic composition (all in wt.%) with  $48 < \text{SiO}_2\% < 52$  and  $2.2 < (\text{Na}_2\text{O}\% + \text{K}_2\text{O}\%) < 3.5$ . But samples from the northern tip of the NS-PSC are, on average, Fe-richer and Qz-normative compared with those coming from the central part of the NS-PSC and from the N15-segment which are Ol-normative. However, major elements plotted against MgO reveal slight variations that define several geochemical groups (Fig. 3): a first one for the basalts from the northern tip of the NS-PSC (both axial and off-axis samples) is characterized by clear liquid lines of descent as MgO varies from 8.7 to 5.2 wt.%, with CaO and  $\text{Al}_2\text{O}_3$  contents respectively down to 9.9 and 12.6 wt.%; a second one for the samples from the central part of the NS-PSC (grey field in Fig. 3) displays a smaller variation of MgO from 8.3 to 7.4 wt.% and higher  $\text{TiO}_2$ ,  $\text{K}_2\text{O}$  or  $\text{Na}_2\text{O}$  contents. And finally, the evolution of the compositions of samples from the N15-segment is different (dotted field in Fig. 3): MgO varies in a small range and  $\text{TiO}_2$ ,  $\text{FeO}^*$ ,  $\text{P}_2\text{O}_5$ ,  $\text{Al}_2\text{O}_3$  and  $\text{K}_2\text{O}$  increase faster when MgO decreases.

The different trends could result from distinctive magmatic series. For each one, the mineral phases subtracted from the liquid, to evolve from one composition to another, would be mostly plagioclase, olivine and to a lesser amount clinopyroxene. Fractionation of plagioclase is even attested with a  $\text{Eu}/\text{Eu}^* < 1$  for all the samples. Titanomagnetite, absent as phenocryst, does not fractionate what is consistent with the enrichment in titanium and iron of the magmas as the MgO content decreases. The different features of geochemical evolution of the two first groups are consistent with a distinction of behavior between two parts of the NS-PSC. The differentiation

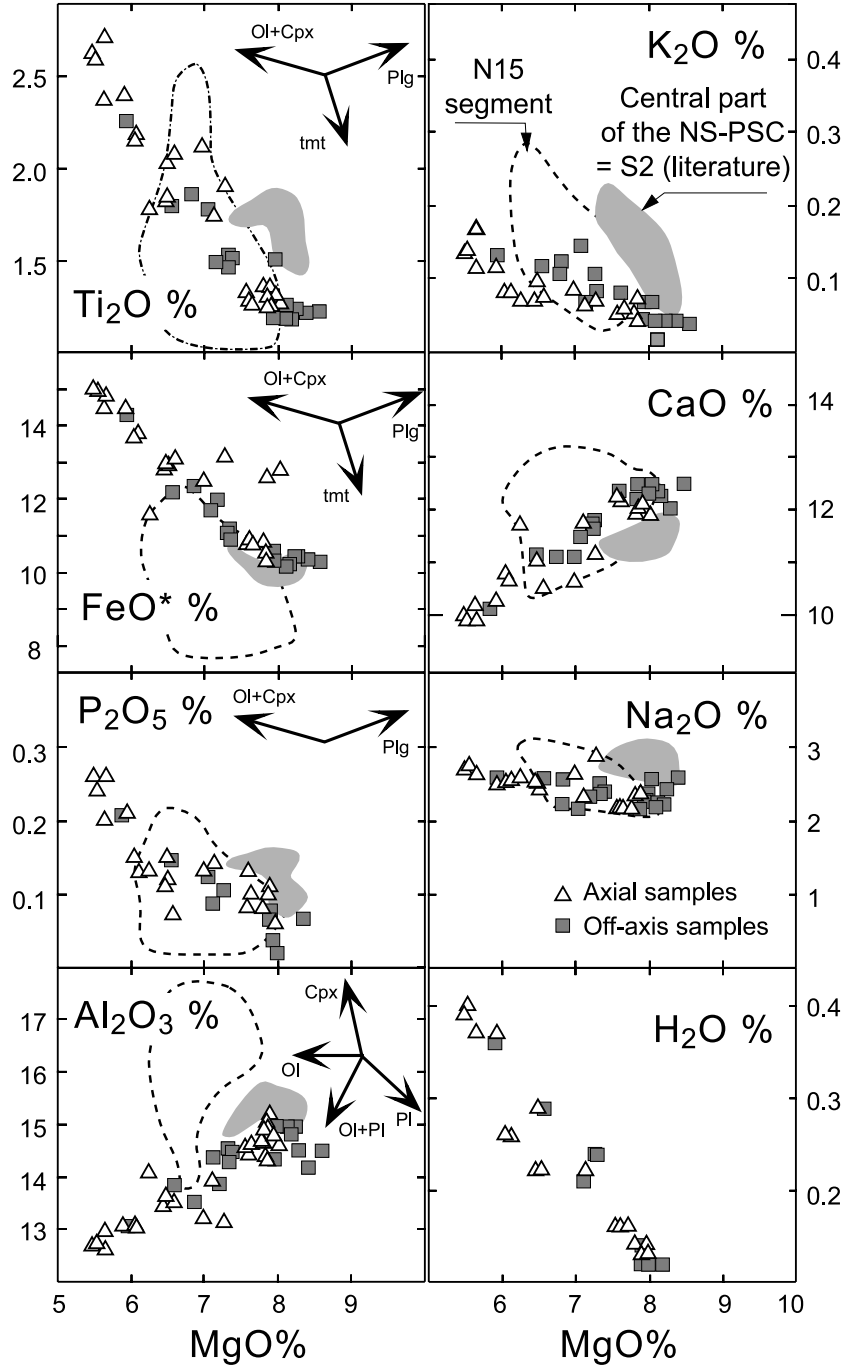


Fig. 3. Major element concentrations plotted *versus* MgO. All analyses in wt.%. Open triangles: samples collected at the axial zone; grey squares: off-axis samples; grey field: central part of the NS-PSC; dotted field: N15-segment (data from *Eissen et al.*, 1991, 1994; *Danyushevsky et al.*, 1993). *Ol* olivine, *Plg* plagioclase, *Cpx* clinopyroxene, *tmt* titanomagnetite

index is maximal on the northern tip ( $Mg\# = 48$ ), with the eruption of Fe–Ti basalts (*Fleutelot et al.*, 1996). These Fe–Ti basalts are the most phyrlic basalts of all the samples containing 20–25 vol.% of phenocrysts in modal composition.

Water behaves as an incompatible element and increases with decreasing MgO. None of the basalts shows any abnormal  $\text{H}_2\text{O}$  enrichment ( $\text{K}_2\text{O}/\text{H}_2\text{O} < 0.5$ ), as already observed for back-arc basin basalts (*Danyushevsky et al., 1993*).

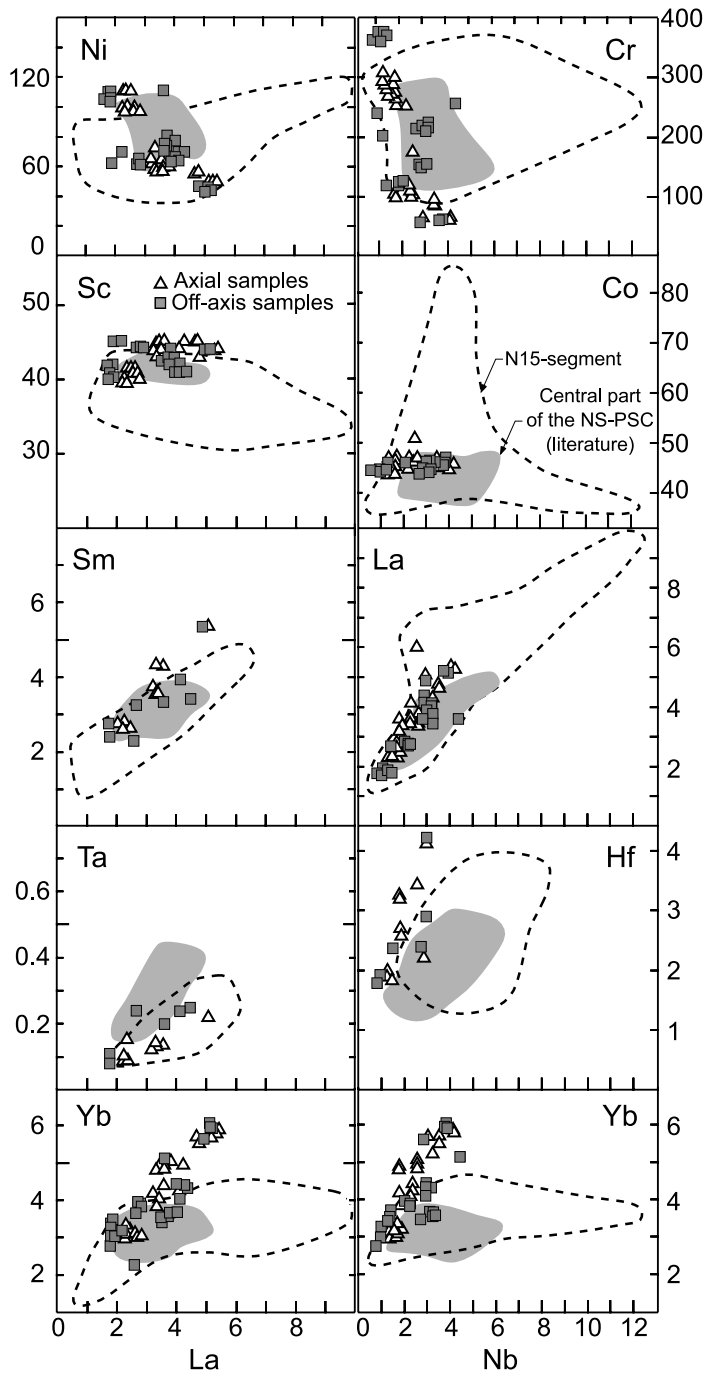


Fig. 4. Trace and rare earth element composition *versus* La and Nb. All analyses in ppm

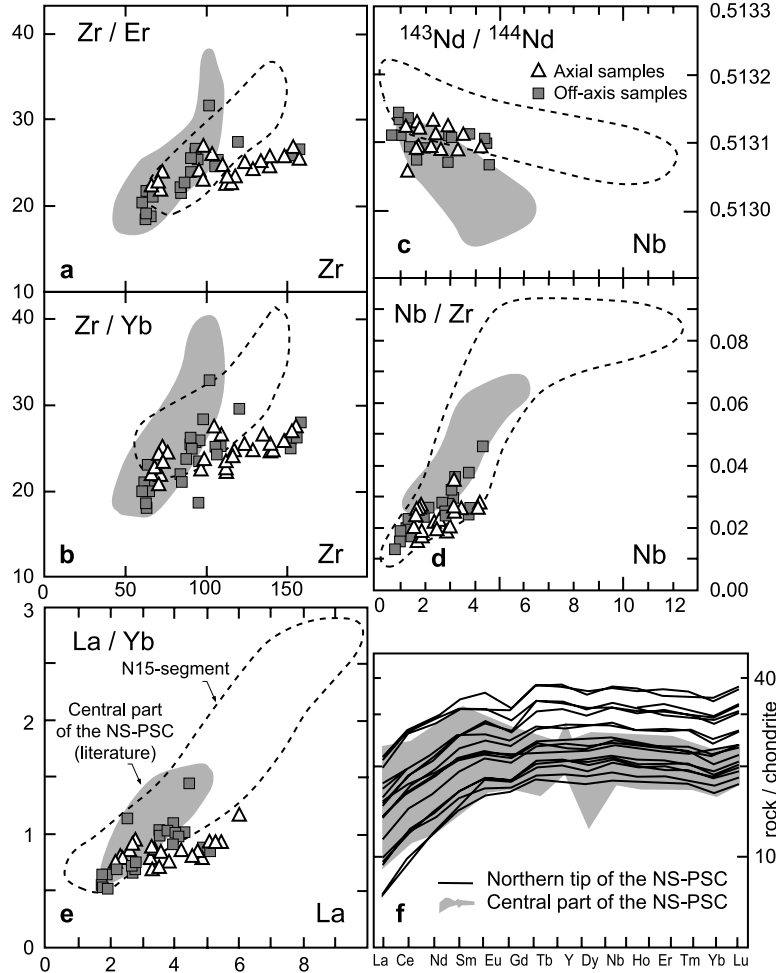


Fig. 5. Trace element ratios (**a**, **b**) versus Zr. Nd isotopic ratio (**c**) versus trace Nb. Trace element ratio versus Nb (**d**) or La (**e**). Same symbols as Fig. 3. Chondrite-normalized rare earth element patterns (**f**) of collected samples from segment S1 of NS-PSC. The grey field represents the patterns from the samples coming from the central part of the NS-PSC (Eissen et al., 1991, 1994; Price et al., 1990; Nohara et al., 1994a, b). Normalization values from Sun and MacDonough (1989)

#### Trace and rare earth elements and isotopic ratios

Geochemical results are presented as a function of La and Nb (Fig. 4) and using trace or isotopic ratios plots and spidergrams (Fig. 5). They define two different kinds of magmatic evolution related to the geographical provenance of the samples: Type A and B samples are from the northern tip and the central part of the NS-PSC, respectively.

Type A is characterized by:

- 1) a wide MgO range (5.2–8.7 wt.%) and the presence of basalts to Fe–Ti basalts (Fig. 3);
- 2) more constant Ta ( $0.19 \pm 0.09$ ) contents (Fig. 4);

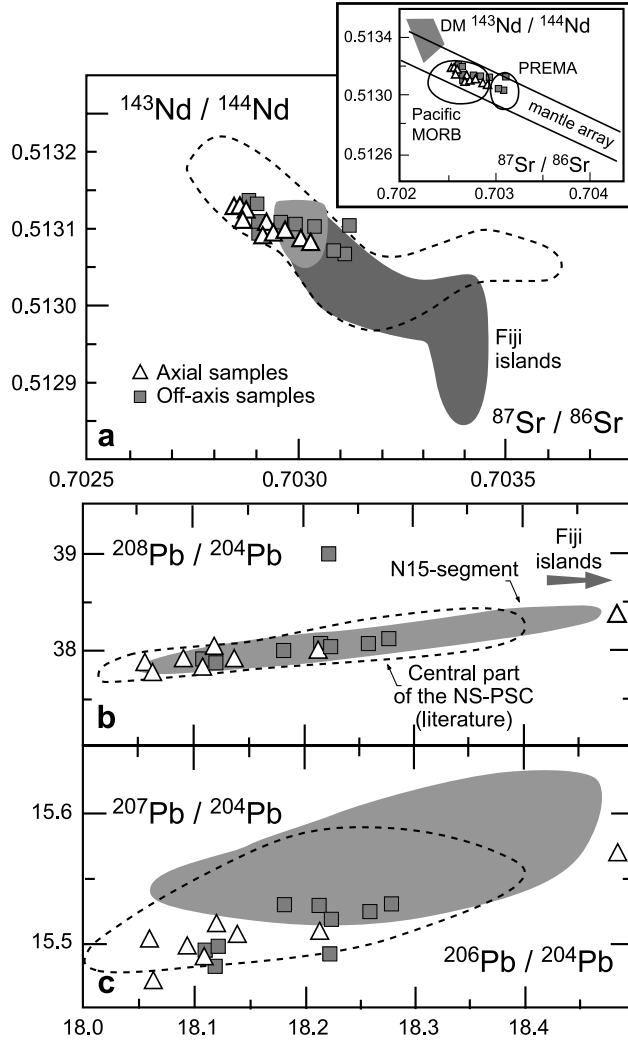


Fig. 6.  $^{143}\text{Nd}/^{144}\text{Nd}$  versus  $^{87}\text{Sr}/^{86}\text{Sr}$  isotopic ratios (a),  $^{208}\text{Pb}/^{204}\text{Pb}$  versus  $^{206}\text{Pb}/^{204}\text{Pb}$  (b) and  $^{207}\text{Pb}/^{204}\text{Pb}$  versus  $^{206}\text{Pb}/^{204}\text{Pb}$  (c) isotopic ratios

- 3) more variable Sm ( $4.0 \pm 1.5$ ), Yb (2.1–6.3), Hf ( $3.0 \pm 1.5$ ) Cr and Ni contents (Fig. 4);
- 4) more constant incompatible element ratios (*e.g.*  $\text{La}/\text{Yb} = 0.8 \pm 0.3$ ;  $\text{Nb}/\text{Zr} = 0.24 \pm 0.05$ ; Figs. 5d, e);
- 5) spidergrams more depleted in LREE (Fig. 5f);
- 6) constant  $^{143}\text{Nd}/^{144}\text{Nd}$  ratios ( $\sim 0.5131$ ) and narrower ranges of  $^{87}\text{Sr}/^{86}\text{Sr}$  (0.7028–0.7031) and  $^{206}\text{Pb}/^{204}\text{Pb}$  ratios (18.05–18.30) (Figs. 5c and 6).

Type B is characterized by:

- 1) a narrow MgO range (7.1–8.2 wt.%) shifted towards higher values (Fig. 3);
- 2) more constant Sm ( $3.2 \pm 0.8$ ), Yb ( $3.2 \pm 1.0$ ) and Hf ( $2.1 \pm 0.6$ ) contents (Fig. 4);
- 3) more variable Ta ( $0.30 \pm 0.15$ ) contents (Fig. 4);
- 4) more variable incompatible element ratio *e.g.*  $\text{La}/\text{Yb}$  ( $1.1 \pm 0.6$ ),  $\text{Nb}/\text{Zr}$  ( $0.45 \pm 0.25$ ) (Figs. 5d, e);

- 5) spidergrams less depleted for LREE (Fig. 5f);
- 6) more variable  $^{143}\text{Nd}/^{144}\text{Nd}$  ratios and higher  $^{207}\text{Pb}/^{204}\text{Pb}$  ratios (Figs. 5c, 6a, c).

Sample of the N15-segment present similarities for both types. There are characterized by:

- 1) a narrow MgO range (7.1–8.2 wt.%) shifted towards higher values (Fig. 3);
- 2) more variable compatible (Ni, Sc, Cr, Ni) and incompatible (La, Yb, Sm) elements (Fig. 4);
- 3) higher variations in incompatible element ratios *e.g.* La/Yb ( $2.0 \pm 1.5$ ), Nb/Zr ( $0.50 \pm 0.42$ ) (Figs. 5d, e);
- 4) much larger ranges of  $^{87}\text{Sr}/^{86}\text{Sr}$  and  $^{143}\text{Nd}/^{144}\text{Nd}$  ratios (Fig. 6a);
- 5) a wider variability of the spidergrams (not presented) with N-type MORB and BABB affinities (with *e.g.* Nb negative anomaly).

## Discussion

Basaltic samples from the central S2 segment and southern part of the S1 segment of the NS propagator (Fig. 7) have a different geochemical signature from those of the northern segment S1: they are characterized by 1) less variation in MgO, shifted towards high values (Fig. 3); 2) variable LREE/HREE ratios (Fig. 5e); and 3) variable Sr and Nd isotopic ratios that are however still within the N-type-MORB field (Fig. 7a, b). Therefore, fractional crystallization alone cannot describe the evolution of such non-cogenetic samples which show, however, a restricted differentiation range.

### *Partial melting processes*

The central segment of the NS-PSC produces only Ol-normative tholeiitic basalts. Mg# values (56–63) of these samples do not characterize a differentiation series towards evolved compositions such as Fe–Ti-basalts. This relatively constant Mg# is not correlated with the constant incompatible element concentration as their variation range is at least equal to that of samples from the northern tip. On the other hand, compatible element concentrations such as Ni, Cr, V, Sc and Co stay relatively constant as the incompatible element concentrations increase. These features cannot be explained by fractional crystallization, which, basically, enriches the magmatic liquids in incompatible elements while it depletes them in compatible elements. However, a partial melting process could explain the relatively constant compatible element concentrations associated with variable concentrations of incompatible elements. But if this is the case, the problem of the variations of isotopic and incompatible element ratios still has to be solved.

Variations of the  $\text{Ca}_8/\text{Al}_8$  ratio (Niu and Batiza, 1991) plotted along axis of the NS-PSC (Fig. 7d) indicate that the melting extent calculated after Niu and Batiza (1991) is higher and more variable for the central part (13–22%) than for the northern tip (13–16%). For the central part of the NS-PSC, the initial pressure of melting ( $P_0$ ), calculated according to the method of Albarède (1992), shows a variation between 0.8 and 1.2 GPa which is on average higher than the 0.7–0.9 GPa range calculated for the northern tip (Fig. 7e).



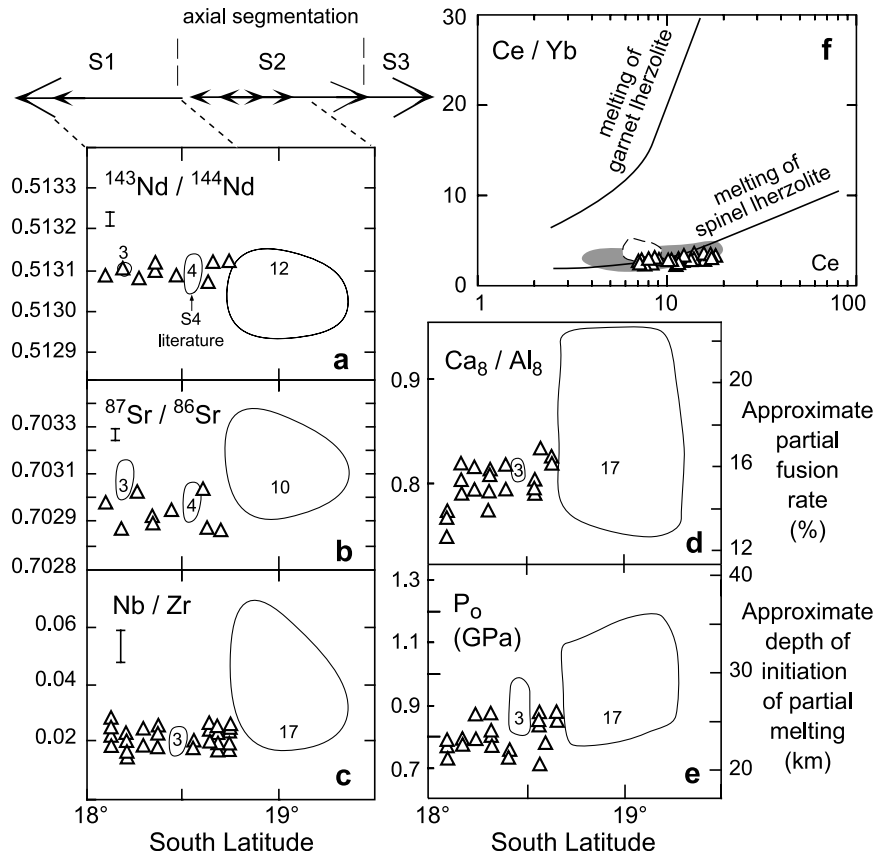


Fig. 7. Along axis variations of different geochemical ratios (a)  $^{143}\text{Nd}/^{144}\text{Nd}$ , (b)  $^{87}\text{Sr}/^{86}\text{Sr}$ , (c)  $\text{Nb}/\text{Zr}$ , (d)  $\text{Ca}_8/\text{Al}_8 = \text{CaO}/\text{Al}_2\text{O}_3$  ratio calculated for a  $\text{MgO}$  concentration of 8 wt.%, according to the method of Klein and Langmuir (1987). This ratio, which erases the fractional crystallization effect, indicates the variations of the melting rate of the mantle because it is not sensitive to the variations of initial pressure of melting (Niu and Batiza, 1994), excepted for high pressures (Klein and Langmuir, 1987); (e)  $P_o$ : initial pressure of partial melting, the empirical equation of Albarède (1992) is based upon  $\text{SiO}_2$  and  $\text{MgO}$  concentration of basalts;  $\text{Ln}P_o \text{ (kbar)} = 0.00252 * [2000 \text{ MgO}/(\text{SiO}_2 + \text{MgO}) + 969] - 0.12\text{SiO}_2 + 5.027$ ; (f)  $\text{Ce}/\text{Yb}$  versus  $\text{Ce}$ . Error bar is 2s. Open triangles are samples collected at the axial zone, open field S4 literature: data from the literature (Eissen et al., 1991, 1994; Nohara et al., 1994; Boespflug et al., 1989). The number given within a field indicates the number of data used to define it

The mineralogy of the mantle, which undergoes melting along the axis of the propagator, seems to be homogeneous along the axis; The weak variation of  $\text{Ce}/\text{Yb}$  ratio versus  $\text{Ce}$  (Fig. 7f) observed is consistent with melting in the spinel-lherzolite field (Niu, 1997). Moreover, a pressure-temperature diagram of partial melting conditions of peridotites (after Jaques and Green, 1980; not shown) indicates that the thermo-barometric conditions evaluated according to Albarède (1992) for the samples from the central part of the propagator fall within the spinel peridotites field.

Therefore, basalts from the NS-PSC are the liquids resulting of partial melting of a mineralogically homogeneous spinel-lherzolite mantle. However, small variations are observed in the trace elements ratios (*e.g.* Nb/Zr; Fig. 5d; La/Yb; Fig. 5e), as well as some isotopic results (Figs. 6, 7) as already mentioned by *Boespflug* (1989, 1990). Variations of both the Nd and Sr isotopic ratios as well as that of some incompatible element ratios (Nb/Zr) which are not fractionated much one to another during partial melting processes have been plotted versus latitude (Fig. 7a–c). The variability of ratios from the central part to the northern tip of the propagator implies a small (generally within the MORB field), but significant geochemical and isotopic heterogeneity of the mantle source (*Eissen et al.*, 1994; *Nohara et al.*, 1994; *Boespflug et al.*, 1989). This heterogeneity results probably of a contamination from the New Hebrides slab, inherited of the rotation of this arc during the opening the NFB as it has been observed on several other segments of this back-arc basin (*e.g.* lower Nb content; *Eissen et al.*, 1994).

#### *Dynamic partial melting beneath the NS-PSC*

*Klein and Langmuir* (1987, 1989) and *Scarrow and Cox* (1995) proposed a model of adiabatic upwelling in which the mantle is thermally heterogeneous. Therefore, the “hottest” parts of the mantle cross the solidus at a higher pressure (deeper), resulting in a longer time for partial melting and therefore a higher degree of partial melting. The “coldest” parts cross the solidus at a lower pressure (shallower) resulting in a lower partial melting extents. This model implies a dynamic partial melting operating at different depths all along a diapiric column of rising asthenosphere. The along strike variations of calculated depth of initiation of partial melting (Fig. 7e) as well as the variations of partial fusion rate (Fig. 7d) suggest the presence of such a diapir focused underneath the central part of the NS-PSC. This rising column of partial melt is therefore

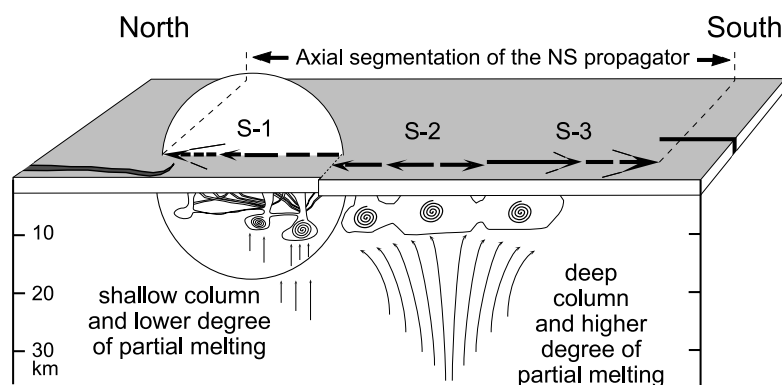


Fig. 8. Schematic longitudinal section of the NS-PSC axis and interpretative view of the petrogenetic processes. The section presents as a sketch the variations in depth of the extend of partial melting as well as the diverse sizes of the shallow magma reservoirs located below each spreading segments. Crystallization processes in magma chambers are discussed and modeled in more detail in *Caroff and Fleutelot* (2003)

sampling the spinel lherzolite mantle and the tapped liquids record the variability of the isotopic ratios and in some incompatible element ratios. Even if the spreading rate is uniform along the NS-PSC (Auzende et al., 1995), the thermal structure of the upper mantle seems to be heterogeneous, resulting in various depths and degree of partial melting. It is significative to notice that the main geochemical shift is observed at the limit between sub-segments S1 and S2 (Figs. 1b, 7). This might reflect clear modification in the magma origin; the depth of initiation of partial melting (Fig. 7e) is deeper ( $\sim 30$  km) below segment S2 than below segment S1 ( $\sim 25$  km) as well as the extend of partial fusion rate; respectively up to 22% versus 16%, or even less towards the propagator tip ( $\sim 12\%$ ).

Therefore, basalts from the central part of the NS-PSC (segments S2 of Fig. 1b) would be the liquids resulting of higher rates and deeper depth of partial melting of a mineralogically homogeneous mantle with a spinel-lherzolite type mineralogy. These observations are consistent with the presence of a permanent, probably relatively large and constantly fed, magma reservoir located below the center of the segment (Fig. 8). However, small variations are observed with trace elements ratio (e.g. Nb/Zr; Fig. 5d; La/Yb; Fig. 5e), as well as some isotopic results (Figs. 6 and 7) as already mentioned by Boespflug (1989, 1990).

#### *Northern tip of the NS-PSC*

The dredged basalts along segment S1 are cogenetic in a broad sense; they exhibit quite constant isotopic and incompatible trace elements ratios, at least in comparison to the basalts from sub-segment S2. Even if all these lavas have normal mid-ocean ridge basalt (N-MORB) mineralogical and geochemical features, three homogeneous compositional groups can be distinguished (Fleutelot et al., 1996); the most differentiated ones being of Fe–Ti basalt composition. Each group, spatially ordered, corresponds to the evolution of individual small magma chambers, of even smaller volume towards the propagator tip (Fig. 8). The petrogenetic mode of such a compositional evolution can be approached by an open system behavior of periodically replenished and tapped steady-state magma chambers (Caroff and Fleutelot, 2003). The two most mafic lava groups were erupted from cyclically periodically replenished magma reservoirs. To allow the differentiation observed, a small volume of the magma migrates along strike between different reservoirs. The differentiation starts within open system reservoirs and ends up in closed system reservoirs as shown by the modellings done by Caroff and Fleutelot (2003). The Fe–Ti basalt group is related to closed system magmatic fractionation in small disconnected magma bodies, located close to the pseudofaults, which end the PSC. In that sense, pseudofaults represent cold walls, which stop the along-axis magma migration. This observation is in agreement with those from Sinton et al. (1983) for the Galapagos and southern Juan de Fuca propagating spreading centers. The variable degree of differentiation may be related to the proximity of pseudofaults and the balance between rate of cooling and supply rate of juvenile magma.

The succession of off-axis valleys and domes suggests a temporal persistence of this kind of magmatic behavior, the duration of each cycle being about 120000

years (*Gracia et al.*, 1996). Thus, the northern part of the NS-PSC seems to have been produced by several magma chambers interconnected by a sill and pipe network (Fig. 8). But along the last 18 km of the northern tip, only isolated smaller magma chambers are present. Consequently the NS-PSC suggests that only a small fraction of magma expelled from each open-system magma chamber actually reaches the surface as lava flows, because a larger fraction of it migrates along strike from one reservoir to another one.

### Summary

The studied set of samples clearly confirms that the NFB has reached a mature stage of magmatic evolution. Indeed, it produces magmas with a signature similar to N-MORB *e.g.* similar to those from the East Pacific Rise with respect to major and trace elements as well as Sr and Nd isotopes (Fig. 6). However, some basalts from the central part of the propagator show more variation in the isotopic ratios, that could be interpreted as the remnant fingerprint of a subduction-related component as has already been noted by *Boespflug* (1990) and *Eissen et al.* (1994), probably inherited from the nearby New Hebrides subduction zone (*Auzende et al.*, 1995). The small variations observed along the central part of the propagator might be related to the fact that the rising asthenosphere is slightly more heterogeneous beneath the central part compared with the tip of the propagator.

A schematic along strike section of the NS-PSC axis with an interpretative view of the petrogenetic processes is proposed in Fig. 8. The long column of dynamic partial melting beneath the central part of the propagator suggests variation in the depth and rate of partial melting. Moreover, a larger volume of magma is expelled in the central area compared with the northern part, attested by the presence of more off-axis seamounts (*Gracia et al.*, 1996).

A quasi similar case has been described from the Mid-Atlantic ridge on the basis of geophysical investigations (*Magde et al.*, 1998). Indeed, small scale seismic tomography identified a low-velocity zone focused beneath the central part of some segments. These segments are pseudo-identical to the V-shaped pattern propagator-type; these are the rhomboedric structures reported by *Gente et al.* (1995). These low-velocity zones are interpreted as “hot” regions with high partial melting rates that suggest the presence of a focused rising asthenospheric diapirs. The petrogenetical evolution proposed is in agreement with the results obtained by *Sinton et al.* (1983) for the Galapagos and southern Juan de Fuca propagating spreading centers.

### Conclusions

- 1) The geochemical variations observed along the NS-PSC of the NFB suggest variations in the petrogenetic processes between the different segments of the NF-PSC.
- 2) Variations along strike are observed on the large and deep scale. Partial fusion started deeper (ca. 30 km) and reached a higher rate (ca. 22%) below the central S2 sub-segment, whereas it starts shallower (ca. 25 km) and at a lower rate

- (ca. 16%) below the northern S1 sub-segment. Dynamic partial melting at different depths of a thermally heterogeneous rising mantle can explain these observations.
- 3) The partial fusion affects a geochemically and isotopically slightly heterogeneous mantle. This heterogeneity is probable inherited from the complex opening history of this back-arc basin, surrounded by subduction zones.
  - 4) At a shallower scale, the magma differentiation takes place within a large and permanent magma reservoir below the central sub-segment S2. On the other hand, along sub-segment S1, the maximum of differentiation occurs right from the tip of the propagator until some 20 km behind it, within periodically closed small magma reservoirs. In order to explain these variations, the presence of an asthenospheric diapir focused beneath the central part of the NS-PSC is proposed.
  - 5) The present results are in agreement with the morphological segmentation observed at the Mid-Atlantic Ridge (*Magde et al.*, 1998) and the petrogenetic evolution proposed for the Galapagos and southern Juan de Fuca propagating spreading centers (*Sinton et al.*, 1983). There is no evidence to distinguish magmatic processes of propagating spreading centers from mature oceanic basins and back-arc basins.

### Acknowledgements

We wish to express our thanks to the captain and crew of the R. V. Alis from the Institut de Recherche pour le Développement (IRD). We acknowledge many constructive discussions with *M. Godart*, *M. Caroff*, *E. Humler*, *J. Escartin*, *J. H. Scarrow* and constructive comments by *C. Wilson* and an anonymous reviewer. This project has been funded by CNRS/INSU through the “Géosciences Marines” program, by the French-Australian cooperation and by the IRD.

### References

- Albarède F* (1992) How deep do common basaltic magmas form and differentiate? *J Geophys Res* 97: 10997–10009
- Alteriis (de) G, Ruellan E, Auzende JM, Ondréas H, Bendel V, Gracia-Mont E, Lagabrielle Y, Huchon P, Tanahachi M* (1993) Propagating rift in the North Fiji Basin (Southwest Pacific). *Geology* 21: 583–586
- Auzende JM, Lafoy Y, Marset B* (1988) Recent geodynamic evolution of the North Fiji Basin (SW Pacific). *Geology* 16: 925–929
- Auzende JM, Eissen JP, Lafoy Y, Gente P, Charlou JL* (1988) Seafloor spreading in the North Fiji Basin (Southwest Pacific). *Tectonophysics* 146: 317–351
- Auzende JM, Hey RN, Pelletier B, Rouland D, Lafoy Y, Gracia E, Huchon P* (1995) Propagating rift west of the Fiji archipelago (North Fiji Basin – SW Pacific). *J Geophys Res* 100: 17823–17835
- Boespflug X* (1990) Evolution géodynamique et géochimique des bassins arrière-arcs. Exemples des bassins d’Okinawa, de Lau et Nord-Fidjien. Thesis, Université de Bretagne Occidentale, Brest, France, 354 pp
- Boespflug X, Dosso L, Bougault H, Joron JL, Calvez JY* (1989) Back-arc basin evolution: a geochemical approach (trace elements and Sr–Nd–Pb isotopes). *EUG V*, Strasbourg, Terra Nova (Special Issue)

- Caroff M, Fleutelot C* (2003) The North–South propagating spreading center of the North Fiji Basin – modeling of the geochemical evolution in periodically replenished and tapped magma chambers. *Mineral Petrol* 79: 203–224
- Ceuleneer G, Rabinowicz M* (1992) Mantle flow and melt migration beneath oceanic ridges: models derived from observations in ophiolites. In: *Phipps Morgan J, Blackman DK, Sinton JM* (eds) Mantle flow and melt generation at Mid Ocean Ridges. AGU Geophys Monogr 71: 123–154
- Chase CG* (1971) Tectonic history of the Fiji plateau. *Geol Soc Am Bull* 82: 3087–3110
- Christie DM, Sinton JM* (1981) Evolution of abyssal lavas along propagating segments of the Galapagos spreading center. *Earth Planet Sci Lett* 56: 321–335
- Cotten J, Le Dez A, Bau M, Caroff M, Maury RC, Dulski P, Fourcade S, Bohn M, Brousse R* (1995) Origin of anomalous rare-earth element and yttrium enrichments in subaerially exposed basalts: evidence from French Polynesia. *Chem Geol* 119: 115–138
- Danyushevsky LV, Falloon TJ, Sobolev AV, Crawford AJ, Carroll M, Price RC* (1993) The H<sub>2</sub>O content of basalt glasses from Southwest Pacific back-arc basins. *Earth Planet Sci Lett* 117: 347–362
- Dosso L, Hanan BB, Bougault H, Schillig JG, Joron JL* (1991) Sr–Nd–Pb geochemical morphology between 10° N and 17° N on the Mid-Atlantic Ridge – a new MORB isotope signature. *Earth Planet Sci Lett* 106: 29–43
- Drake J, Weill DF* (1975) Partition of Sr, Ba, Ca, Y, Eu<sup>2+</sup>, Eu<sup>3+</sup>, and other REE between plagioclase feldspar and magmatic liquid: an experimental study. *Geochim Cosmochim Acta* 39: 689–712
- Dubois J, Dugas F, Lapouille A, Louat R* (1975) Fossés d’effondrement en arrière de l’arc des Nouvelles-Hébrides. Mécanismes proposés. *Rev Géogr Phys Géol Dyn* 17: 73–94
- Eaby-Dixon J, Clague DA, Eissen JP* (1986) Gabbroic xenoliths and host ferrobasalts from the southern Juan de Fuca Ridge. *J Geophys Res* 91: 3795–3820
- Eissen JP, Lefèvre C, Maillet P, Morvan G, Nohara M* (1991) Petrology and geochemistry of the central North Fiji Basin spreading centre (Southwest Pacific) between 16° S and 22° S. *Marine Geol* 98: 201–239
- Eissen JP, Nohara M, Cotten J, Hirose K* (1994) The North Fiji Basin basalts and their magma sources, part 1. Incompatible element constraints. *Marine Geol* 116: 153–178
- Falvey DA* (1975) Arc reversals, and a tectonic model for the North Fiji Basin. *Austral Soc Explor Geophys Bull* 6: 47–49
- Fleutelot C, Eissen JP, Tonnerre T, Danyushevsky L, Rory V, Mollard L, Juteau T, Cotten J, Bohn M* (1996) Propagation en contexte arrière-arc: premiers résultats de la campagne ProFeTi (Bassin Nord-Fidjien, Pacifique SW). *Compt Rend Acad Sci Paris* 322: 853–860
- Fornari DJ, Perfit MR, Malahoff A, Embley R* (1983) Geochemical studies of abyssal lavas recovered by DSRV Alvin from eastern Galapagos rift, Inca transform, and Ecuador rift. 1. Major element variations in natural glasses and spacial distribution of lavas. *J Geophys Res* 88: 10519–10529
- Gente P, Pockalny RA, Durand C, Deplus C, Maia M, Ceuleneer G, Mével C, Cannat M, Laverne C* (1995) Characteristics and evolution of the segmentation of the Mid-Atlantic Ridge between 20° N and 24° N during the last 10 million years. *Earth Planet Sci Lett* 129: 55–71
- Gilg-Capar L* (1994) Etude des anomalies du géoïde à moyennes longueurs d’onde: implications sur les mécanismes de l’accrétion et l’origine du volcanisme intraplaque. Thesis, Université de Bretagne Occidentale, Brest, France, 289 pp

- Gill JB, Gorton M (1973) A proposed geological and geochemical history of eastern Melanesia. In: Coleman PJ (ed) *The Western Pacific: island arcs, marginal seas and geochemistry*. University of Western Australia Press, Perth, pp 543–566
- Govindaraju K (1994) Compilation of working values and sample description for 383 geostandards. *Geostand News* (Spec Issue) 18: 158 pp
- Gracia E, Tisseau C, Maia M, Tonnerre T, Auzende JM, Lagabrielle Y (1996) Variability of the axial morphology and of the gravity structure along the central spreading ridge (Nord Fiji bassin): evidence for contrasting thermal regime. *Marine Geophys Res* 18: 249–273
- Grove TL, Bryan WB (1983) Fractionation of pyroxene-phyric MORB at low pressure: an experimental study. *Contrib Mineral Petrol* 84: 293–309
- Hey RN (1977) A new class of “pseudofault” and their bearing on plate tectonics: a propagating rift model. *Earth Planet Sci Lett* 37: 321–325
- Hey RN, Sinton JM (1979) New observations and implications of propagating rifts. AGU Fall Meeting. *EOS Trans* 60: 957
- Hey RN, Wilson DS (1982) Propagating rift explanation for the tectonic evolution of the north-east Pacific: the pseudomovie. *Earth Planet Sci Lett* 58: 167–188
- Hey RN, Dunnebie FK, Morgan WJ (1980) Propagating rifts on mid-ocean ridges. *J Geophys Res* 85: 3658–3674
- Hey RN, Kleinrock MC, Miller SP, Atwater TM, Searle RC (1986) Seabeam/deep-tow investigation of an active oceanic propagation rift system, Galapagos 95.5° W. *J Geophys Res* 91: 3369–3393
- Horen H, Fleutelot C (1998) Highly magnetized and differentiated basalts in the North Fiji Basin: new insights into the identification of propagating rifts. *Marine Geophys Res* 20: 129–137
- Jaques AL, Green DH (1980) Anhydrous melting of peridotite at 0–15 kb pressure and the genesis of tholeiitic basalts. *Contrib Mineral Petrol* 73: 287–310
- Johnson HP, Karsten JL, Delaney JR, Davis EE, Currie RG, Chase RL (1983) A detailed study of the Cobb offset of the Juan de Fuca ridge: evolution of a propagating rift. *J Geophys Res* 88: 2297–2315
- Juteau T, Bideau D, Dauteuil O, Manac’h G, Naïdoo DD, Nehlig P, Ondréas H, Tivey MA, Whipple KX, Delaney JR (1995) De la propagation à l’accrétion océanique: étude par submersible du mur nord de la fosse Ouest-Blanco (Zone de fracture Blanco, Pacific NE). *Bull Soc Géol France* 166: 105–121
- Klein EM, Langmuir CH (1987) Global correlations of ocean ridge basalt chemistry with axial depth and crustal thickness. *J Geophys Res* 92: 8089–8115
- Klein EM, Langmuir CH (1989) Local versus global variations in ocean ridge basalt composition: a reply. *J Geophys Res* 94: 4241–4252
- Lewis BTR (1979) Periodicities in volcanism and longitudinal magma flow on the East Pacific Rise at 23° N. *Geophys Res Lett* 6: 753–756
- Malahoff A, Feden RH, Fleming HS (1982) Magnetic anomalies and tectonic fabric of marginal basins north of the New Zealand. *J Geophys Res* 87: 4109–4125
- Manac’h G (1997) Caractérisation de circulations fluides dans la croûte océanique actuelle (Zone de Fracture Blanco) et fossile (Ophiolite d’Oman). Thesis, Université de Bretagne Occidentale, Brest, France, 311 pp
- Nicolas A (1989) Structures of ophiolites and dynamics of oceanic lithosphere. Kluwer Academic Publishers, Dordrecht, 368 pp
- Niu YL, Batiza R (1991) DENSICAL: a program for calculating densities of silicate melts and mantle minerals as a function of pressure, temperature, and composition in melting range. *Comput Geosci* 17: 679–687

- Niu YL (1997) Mantle melting and melt extraction processes beneath ocean ridges: evidence from abyssal peridotites. *J Petrol* 38: 1047–1074
- Nohara M, Hirose K, Eissen JP, Urabe T, Joshima M (1994) North Fiji Basin basalts and their magma sources, part II. Trace element and isotopes constraints. *Marine Geol* 116: 179–195
- Parson LM, Pearce JA, Murton BJ, Hodkinson RA (1990) Role of ridge jumps and ridge propagation in the tectonic evolution of the Lau back-arc basin, southwest Pacific. *Geology* 18: 470–473
- Pelletier B, Lafoy Y, Missègue F (1993) Morphostructure and magnetic fabric of the north-western North Fiji Basin. *Geophys Res Lett* 20: 1151–1154
- Perfit MR, Fornari DJ (1983a) Geochemical studies of abyssal lavas recovered by DSRV Alvin from eastern Galapagos rift, Inca transform, and Ecuador rift, 2. Phase chemistry and crystallization history. *J Geophys Res* 88: 10530–10550
- Perfit MR, Fornari DJ (1983b) Geochemical studies of abyssal lavas recovered by DSRV Alvin from eastern Galapagos rift, Inca transform, and Ecuador rift, 3. Trace element abundances and petrogenesis. *J Geophys Res* 88: 10551–10572
- Phipps Morgan J, Parmentier EM (1985) Causes and rate-limiting mechanisms of ridge propagation: a fracture mechanism model. *J Geophys Res* 90: 8603–8612
- Price RC, Johnson LE, Crawford AJ (1990) Basalts of the North Fiji basin: the generation of back arc basin magmas by mixing of depleted and enriched mantle sources. *Contrib Mineral Petrol* 105: 106–121
- Roeder PL, Emslie RF (1970) Olivine-liquid equilibrium. *Contrib Mineral Petrol* 29: 275–289
- Ruellan E, Huchon P, Auzende JM, Gracia E (1994) Propagating rift and overlapping spreading center in the North Fiji Basin. *Marine Geol* 116: 37–56
- Scarrow JH, Cox KG (1995) Basalts generated by decompressive adiabatic melting of a mantle plume: a case study from the Isle of Skye, NW Scotland. *J Petrol* 38: 3–22
- Sinton JM, Wilson DS, Christies DM, Hey RN, Delaney JR (1983) Petrologic consequences of rift propagation on oceanic spreading ridges. *Earth Planet Sci Lett* 62: 193–207
- Sun SS, MacDonough WF (1989) Chemical and isotopic systematics of oceanic basalts: implication for mantle composition and processes. In: *Saunders AD, Norry MJ* (eds) *Magmatism in the Ocean Basins*. Blackwell Scientific Publications, London (Geol Soc Spec Publ 42: 313–345)
- Thy P (1991) High and low pressure phase equilibria of a mildly alkalic lava from 1965 Surtsey eruption: experimental results. *Lithos* 26: 223–243
- Todt W, Cliff RA, Hanser A, Hoffmann AW (1984)  $^{202}\text{Pb} + ^{205}\text{Pb}$  double spike for lead isotopic analyses. *Terra Cognita* 4: 209
- Ulmer B (1989) Partitioning of high field strength elements among olivine, pyroxenes, garnet and calcalkaline picobasalt: experimental results and an application. *Carnegie Inst Washington Yearb* 88: 42–47
- Wilson DS, Hey RN (1995) History of rift propagation and magnetization intensity for the Cocos-Nazca spreading center. *J Geophys Res* 100: 10041–10056

Authors' addresses: C. Fleutelot, Université de Bretagne Occidentale, Dept. des Sciences de la Terre, UMR 6538 “Domaines Océaniques”, 6 avenue le Gorgeu, BP 809, 29285 Brest Cedex, France; present address: Université de Rennes I, Géosciences Rennes, CNRS UPR 4661, Campus de Beaulieu, Av. du général Leclerc, 35042 Rennes Cedex, France, e-mail: Corinne.Fleutelot@univ-rennes1.fr; J. P. Eissen (corresponding author), IRD UR031 “Processus et Aléas Volcaniques”, A.P. 17-12-857, Quito, Ecuador; present address: IRD UR163 “Processus et Aléas Volcaniques”, Laboratoire Magmas et Volcans, 5, rue Kessler, 63038



Clermont-Ferrand, France, e-mail: Jean-Philippe.Eissen@ird.fr; *L. Dosso* and *C. Bollinger*, UMR 6538 “Domaines Océaniques”, c/o Ifremer, Centre de Brest, BP 70, 29280 Plouzané Cedex, France, e-mail: Laure.Dosso@ifremer.fr; Claire.Bassoullet@ifremer.fr; *T. Juteau* and *J. Cotten*, Université de Bretagne Occidentale, Dept. des Sciences de la Terre, UMR 6538 “Domaines Océaniques”, 6 avenue le Gorgeu, BP 809, 29285 Brest Cedex France, e-mail: juteau@univ-brest.fr; cotten@univ-brest.fr; *P. Launeau*, Université de Nantes, UPRES-EA 2156, Laboratoire de Pétrologie Structurale, 2 rue de la Houssinière BP 92208, 44322 Nantes Cedex, France, e-mail: Patrick.Launeau@chimie.univ-nantes.fr; *L. Danyushevsky*, Department of Geology, University of Tasmania, Box 252-79, Hobart 7001 Tasmania, Australia, e-mail: l.dan@utas.edu.au; *L. Savoyant*, Université de Montpellier II, UMR 5569 “Géofluides, Bassins, Eau,”, 34095 Montpellier Cedex 5, France, e-mail: savoyant@dsu.univ-montp2.fr